MIT Open Access Articles

Large Intermediates in Hydrazine Decomposition: A Theoretical Study of the N_3H_5 and N_4H_6 Potential Energy Surfaces

Massachusetts Institute of Technology

Large Intermediates in Hydrazine Decomposition: A Theoretical Study of the N_3H_5 and N_4H_6 Potential Energy Surfaces

Journal:	*The Journal of Physical Chemistry*
Manuscript ID	jp-2019-02217p.R1
Manuscript Type:	Article
Date Submitted by the Author:	n/a
Complete List of Authors:	Grinberg Dana, Alon; Massachusetts Institute of Technology, Chemical Engineering Moore, Kevin; Argonne National Laboratory, Gas Phase Chemical Dynamics Jasper, Ahren; Argonne National Laboratory, Gas Phase Chemical Dynamics Green, William; Massachusetts Institute of Technology, Chemical Engineering

SCHOLARONE™
Manuscripts

1
2
3
4
5
Large Intermediates in Hydrazine Decomposition: A Theoretical Study of the

N₃H₅ and N₄H₆ Potential Energy Surfaces

Alon Grinberg Dana[1], Kevin B. Moore III,[2] Ahren W. Jasper,[2] William H. Green[1]*

[1] Department of Chemical Engineering, Massachusetts Institute of Technology, Cambridge, MA 02139, United States

[2] Chemical Sciences and Engineering Division, Argonne National Laboratory, Argonne, IL 60439, United States

* Corresponding author. Email: whgreen@mit.edu; Fax: +1-617-324-0066; Tel: +1-617-253-4580

1

Abstract

Large complex formation involved in the thermal decomposition of hydrazine (N_2H_4) is studied

using transition state theory based theoretical kinetics. A comprehensive analysis of the N_3H_5 and

N_4H_6 potential energy surfaces was performed at the CCSD(T)-F12a/aug-cc-pVTZ//ωB97x-D3/6-

311++G(3df,3pd) level of theory, and pressure-dependent rate coefficients were determined.

There are no low-barrier unimolecular decomposition pathways for triazane (n-N_3H_5), and its

formation becomes more significant as the pressure increases; it is the primary product of N_2H_3

+ NH_2 below 550, 800, 1150, and 1600 K at 0.1, 1, 10, and 100 bar, respectively. The N_4H_6 surface

has two important entry channels, N_2H_4 + H_2NN and N_2H_3 + N_2H_3, each with different primary

products. Interestingly, N_2H_4 + H_2NN primarily form N_2H_3 + N_2H_3, while disproportionation of N_2H_3

+ N_3H_3 predominantly leads to the other N_2H_2 isomer, HNNH. Stabilized tetrazane (n-N_4H_6)

formation from N_2H_3 + N_2H_3 becomes significant only at relatively high pressures and low

temperatures due to fall-off back into N_2H_3 + N_2H_3. Pressure-dependent rate coefficients for all

considered reactions as well as thermodynamic properties of triazane and tetrazane, which

should be considered for kinetic modeling of chemical processes involving nitrogen- and

hydrogen-containing species, are reported.

2

1. Introduction

Hydrazine (N_2H_4), the main component of diamine-based rocket fuels, is an excellent propellant: using oxygen as the oxidizer, it is only second to hydrogen in terms of the specific impulse (thrust developed per fuel mass per unit time) it generates.[1] Its decomposition could lead to auto-ignition and detonation,[2–4] and it is sometimes used as a monopropellant, usually by decomposing over a catalyst.[1] Hydrazine and hydrazine-based fuels such as monomethyl hydrazine are more commonly used as bipropellants with N_2O_5 as the oxidizer. Hydrazine is used in thruster engines for attitude and in-orbit control of satellites and spacecraft,[1] where it is being stored and utilized at a maximal pressure of about 25 bar.[5–7]

No detailed kinetic models for hydrazine-based fuels combustion in N_2O_5 exist in the current literature; a step towards this goal is understanding hydrazine decomposition better. Detailed kinetic models for hydrazine decomposition were previously suggested by Halat-Augier et al.[8] as well as by Konnov and De Ruyck.[9] More recently, however, computations of the N_2H_2,[10,11] N_2H_3,[11] and N_2H_4[10–12] potential energy surfaces determined updated kinetics. Interestingly, none of the previous works on hydrazine decomposition has considered species containing more than two nitrogen atoms. In the absence of an oxidizer, a monopropellant's decomposition could be thought of as an extreme case of fuel-rich combustion, a chemistry region in which fuel-radical recombination reactions often play a significant role. At low pressures, chemically-activated isomerization and decompositions are often important. As the working pressure increases, radical recombination reactions, leading to formation of relatively large complexes, become more significant due to collisional stabilization.

3

Unlike carbon, nitrogen does not normally form the major elemental backbone of large molecules. For example, an experimental study of tetrazene (linear unsaturated N_4H_4) determined that its thermolysis in the solid phase begins at room temperature, while in the gas phase it is metastable.[13] Moreover, cyclic nitrogenous rings, and specifically tetrazetidine (cyclic N_4H_4), were determined to have relatively high ring strain energies.[14–16] However, a theoretical study of triazane (N_3H_5) concluded that it is kinetically stable.[17] Tetrazane (saturated N_4H_6) was also studied theoretically, and its most stable stereoisomer was determined,[18] yet its overall kinetic stability was not assessed. A sub-atmospheric room temperature experimental observation of N_2H_3 self-reaction concluded that the disproportionation reaction yielding N_2H_4 + N_2H_2 is approximately four times faster than a recombination reaction yielding tetrazane, unlike the tendency of the analogous hydrocarbon radical, C_2H_5.[19] Yet the behavior of the N_2H_3 + N_2H_3 system at high temperatures and different pressure, and specifically the importance of well-skipping chemically-activated reactions, has not been reported in the literature.

In the present contribution, we examine the hypothesis that abundant radicals in decomposing hydrazine might form relatively large complexes such as triazane and tetrazane, becoming more significant as the pressure increases. We therefore explore the NH_2 + N_2H_3 and N_2H_3 + N_2H_3 reactions which lead to pressure-dependent kinetic networks on the N_3H_5 and N_4H_6 potential energy surfaces, respectively. Specifically, collisional-stabilized formation of the complexes along with well-skipping reactions are considered, and pressure-dependent rate coefficients are determined.

4

2. Theoretical methods

2.1. Characterizing the Potential Energy Surface

Geometric structures and vibrational frequencies for all wells and saddle points considered here were obtained using density functional theory employing the ωB97x-D3 functional[20] and the 6-311++G(3df,3pd) basis set.[21] The growing string method (GSM)[22] was used to provide initial guesses for some of the transition state geometries. Intrinsic reaction coordinate (IRC) calculations[23] were used to verify all transition state configurations by tracking the minimum energy paths leading to adjacent local minima.

Higher level single-point energies were obtained by employing the explicitly correlated coupled-cluster CCSD(T)-F12a method[24,25] and using an augmented Dunning's correlation consistent, polarized valence triple-ζ (aug-cc-pVTZ) basis set.[26] Zero-point energy (ZPE) corrections, incorporated into the final energies reported here, were evaluated at the ωB97x-D3/6-311++G(3df,3pd) level and scaled by a recommended factor of 0.970[27] to account for their average overestimation, due in part to anharmonicity. Previously, Hwang and Mebel[10] showed that CCSD(T)/6-311G(d,p) level energies are reliable (do not deviate by more than 2 kcal mol^{-1} from respective multireference CASSCF calculations using the full valence active space) for similar N/H systems on the N_2H_4 potential. The comparison included the iminoammonium (NH_3NH) species, a zwitterionic compound similar in structure to other zwitterions discussed in the present work. A high value of the T1 diagnostic parameter[28] implies that additional dynamic electron correlation retrieved by a multireference method is significant. At the CCSD(T)-F12a/aug-cc-pVTZ level, the T1 value for NH_3NH is 0.0112, similar to the T1 range of the various

5

stable species reported in the present work (0.0090–0.0151). However, radicals such as N_2H_3 and N_3H_4 have higher T1 values in the range of 0.0211 – 0.0247, indicating a larger uncertainty in their energies.

Starting from the optimized geometries, separate relaxed potential energy scans were performed as a function of the dihedral angle around each single bond for all stationary points on the potential energy surface (PES). All scans had a 10° increment resolution, unless otherwise noted. These hindered rotor scans were performed using density functional theory employing the Becke-3-Lee-Yang-Parr (B3LYP) functional[29] and the 6-311++G(3df,3pd) basis set.[21] The potential energies were fitted to truncated Fourier series, and used as input to Arkane, an open-source master equation (ME) transition state theory (TST) solver included within the Reaction Mechanism Generator (RMG) suite,[30,31] to compute the partition functions. The potential scans are given in the Supporting Information (Figs S1–S10). The optimized geometry was verified to have the lowest energy on these potential scans.

Q-Chem 4.4.0[32] was used for geometry optimizations and frequency calculations. Molpro 2015.1[33,34] was used for coupled-cluster electronic energy calculations. Gaussian[35] was used for all dihedral angle rotor scans, IRC, and GSM calculations. Radical species were computed using unrestricted methods. IQmol[36] was used to plot molecular orbitals generated using the NBO 6.0 population analysis software[37].

2.2. Calculating thermodynamic parameters

Energies at zero K (E0) of n-N_3H_5, n-N_3H_4, i-N_3H_4, and n-N_4H_6 were compared using three computational methods. First, the composite CBS-QB3 method[38] was considered; the reported error bar of the CBS-QB3 method is 13.0 kJ mol^{-1}.[39] A recommended ZPE correction scaling factor

6

of 0.99[40] was used for this method. The level of theory used throughout this work to characterize the potential energy surfaces and calculate kinetic rate coefficients, CCSD(T)-F12a/aug-cc-pVTZ//ωB97x-D3/6-311++G(3df,3pd), was also used. A ZPE correction scaling factor of 0.970 was adopted for this method.[27] A similar method with a different basis set for the single point calculation, CCSD(T)-F12a/cc-pVTZ-F12//ωB97x-D3/6-311++G(3df,3pd), was also implemented. Here, a ZPE correction scaling factor of 0.984 was used.[41,42] Only the CCSD(T)-F12a/cc-pVTZ-F12 method was used for thermodynamic data calculations since it has available bond additivity corrections (BAC) in Arkane.

2.3. Calculating kinetic parameters

Both high-pressure (P) limit and P-dependent thermal rate coefficients, k(T) and k(T,P), were calculated at CCSD(T)-F12a/aug-cc-pVTZ//ωB97x-D3/6-311++G(3df,3pd) using Arkane. Values of k(T) for every elementary chemical reaction which has an energy barrier were calculated by a TST analysis[43] using the rigid-rotor harmonic oscillator (RRHO) approximation with low-energy (< 40 kJ mol^{-1} barrier) internal rotations modelled as one-dimensional hindered rotors (1D-HR). The effect of internal rotation(s) on the harmonic frequencies was eliminated by projection.[44] One-dimensional asymmetric tunneling through tight transition states was incorporated by assuming that the reaction path can be described by an Eckart function.[45] Phenomenological k(T,P)'s were computed by applying the microcanonical RRKM (Rice–Ramsperger–Kassel–Marcus) theory to solve the ME[46] under the modified strong collision (MSC) approximation (RRHO and 1D-HR approximations were also used in calculating densities of states).[47] Calculations were performed at a mesh of (T_i, P_j) points, and the k(T_i, P_j) fitted to a Chebyshev polynomial suitable for use in Cantera[48] or the commercial version of Chemkin[49]. The reported rate coefficients incorporate

7

appropriate degeneracy factors. For barrierless pathways, high-P k(T)'s estimates (either using literature data or estimated by the respective RMG template) were input into Arkane and converted into k(E)'s for solution of the ME using an inverse Laplace transform.[47] As is usually done when constructing the ME, the input channel was treated as pseudo-first-order and dissociations into bimolecular products in P-dependent networks were treated as irreversible. The rates of collisional energy transfer (CET) for deactivating collisions were modeled using the "single exponential down" expression:

$$P\left(E \leftarrow E'\right) \propto \exp\left(-\frac{E'-E}{<\Delta E_d>}\right), \qquad E' > E$$

where $<\Delta E_d>$ is a measure of the collision efficiency. We computed $<\Delta E_d>$ for $N_3H_5 + N_2$ and $N_4H_6 + N_2$ at several temperatures using classical trajectory approaches[50–52] and potential energy surface construction strategies[53] described in detail elsewhere. The trajectory-based results are well-represented (to better than 10%) by the expressions $<\Delta E_d>$ = 175 (T/298 K)$^{0.52}$ cm^{-1} and $<\Delta E_d>$ = 250 (T/298 K)$^{0.30}$ cm^{-1} from T = 300 to 3000 K for $N_3H_5 + N_2$ and $N_4H_6 + N_2$, respectively. The calculated values of $<\Delta E_d>$ for the two systems are similar at high *T*, while $<\Delta E_d>$ is larger for N_4H_6 than for N_3H_5 at low *T*. These trends are consistent with those reported previously for hydrocarbons and several bath gases,[54] where we also showed that trajectory-based values of $<\Delta E_d>$ often have a weaker temperature dependence than the $T^{0.85}$ appearing in the empirical standard expression.[55] In addition to uncertainties arising from the value of $<\Delta E_d>$, errors in the present collision model may be attributed to simplifications in the expression for *P(E←E')* given above and to the neglect of rovibrational anharmonicity when evaluating the density of states near threshold.[52] Altogether, we often find empirically (e.g., for methane,[56] propargyl radical,[57] and 2-methyl-allyl radical[58]) that the use of the single exponential down model

8

along with trajectory-based values of $<\Delta E_d>$ predicts k_0 with errors of a factor of two or less, thanks in part to a cancellation of errors when rovibrational anharmonicity is neglected.

Transport parameters (Lennard-Jones parameters, dipole moment, and polarizability) were calculated using the OneDMin code,[59] Molpro, and Gaussian. These Lennard-Jones parameters (well depth and collision diameter) are also necessary for pressure-dependent rate calculations, specifically for the collision frequency calculation. Lennard-Jones parameters were calculated using a DF-MP2/aug-cc-pVDZ potential energy surface with N_2 as the collider. Similar calculations (MP2/aug-cc-pVDZ) were previously shown to be within 10% of the more accurate MP2/CBS and QCISD(T)/CBS computations;[59] similar errors were found in tests of this approach against experimental and higher-level theoretical diffusion coefficients.[60] The dipole moment and polarizability parameters were computed at the B2PLYPD3/cc-pVTZ level. All transport parameters are given in the Supporting Information (Table S1).

Network sensitivity analysis was conducted using Arkane by perturbing each of the relevant wells and transition states in the potential energy surface, and determining the effect on the calculated pressure-dependent rates.

9

3. Results and Discussion

3.1. The N_3H_5 system

An N3 isomer with the empirical chemical formula N_3H_5 could be generated in systems with relatively high concentrations of N_2H_3 and NH_2 radicals. This N_3H_5 potential energy diagram describes several ammonia-forming pathways (Fig. 1). It consists of a pressure-dependent network on the singlet surface (Fig. 1) with two isomers, n-N_3H_5 (triazane, NH_2NHNH_2) and 1,2-z-N_3H_5 (NH_2NH_2NH) (Fig. 2), as well as bimolecular pathways on both the singlet and triplet surfaces. The 'n' and 'z' in the species names above stand for normal and zwitterion, respectively. Geometric representations of relevant species and saddle points are given in Figs. 2 and 3, respectively. Table 1 lists point groups, rotational constants, and unscaled harmonic frequencies for all relevant species and transition states.
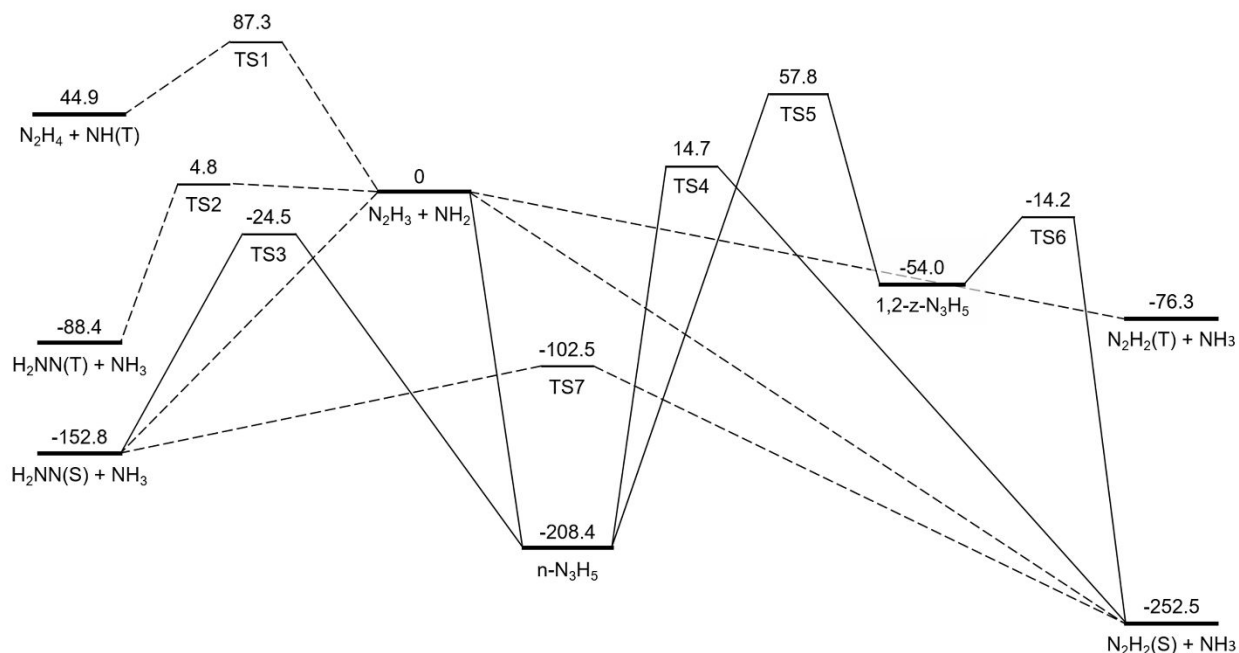

Figure 1. Reaction path diagram for the N_3H_5 PES. Dashed lines represent non-pressure-dependent pathways. (S) and (T) represent singlet or triplet multiplicities, respectively. Energies are in kJ mol^{-1}, and scaled relative to the $N_2H_3 + NH_2$ entry channel, which was set at zero.

10

The entry channel of the pressure-dependent network, N_2H_3 + NH_2, leads via the n-N_3H_5 intermediate to two lower-energy bimolecular exit channels, each consists of an N_2H_2 isomer and ammonia. The barrierless high pressure limit rate for the complex formation reaction, N_2H_3 + NH_2 $\leftrightarrow$ n-N_3H_5 (Reaction B1, Table 2), was assumed to equal the rate of a similar reaction, CH_3NH + NH_2 $\leftrightarrow$ CH_3NHNH_2, calculated at the CASPT2/aug-cc-pVDZ level.[61] For simplicity, highly energetic wells were excluded from the PES. For example, N_2H_2 + NH(S) formed barrierlessly from 1,2-z-N_3H_5 is 192.0 kJ mol^{-1} above the N_2H_3 + NH_2 entry channel.

The N_2H_2(S) + NH_3 product well is the most stable product channel in Fig. 1, yet the pathway forming the H_2NN(S) + NH_3 product well has a lower barrier (Fig. 1). Nevertheless, all barriers surrounding n-N_3H_5 are relatively high; consequently, even moderate pressures would be enough for the excited complex to be stabilized as n-N_3H_5.

Table 1. Point Groups, Rotational Constants and Unscaled Vibrational Frequencies Calculated at the ωB97x-D3/6-311++G(3df,3pd) Level of Theory for Stationary Points on the N_3H_5 PES

stationary point	point group	rotational constants (cm^{-1})	harmonic frequencies (cm^{-1})
NH(T)	$C_{\infty v}$	16.66	3326.8
NH_2	C_{2v}	23.77, 12.93, 8.37	1519.9, 3418.0, 3510.4
NH_3	C_{3v}	10.02, 10.02, 6.31	1030.0, 1664.9, 1677.8, 3518.4, 3644.2, 3644.2
H_2NN(S)	C_{2v}	11.18, 1.34, 1.18	1016.2, 1342.2, 1642.3, 1735.5, 3154.9, 3165.2
H_2NN(T)	C_s	10.02, 1.13, 1.05	727.2, 1102.3, 1265.6, 1587.7, 3448.1, 3555.2
N_2H_2(S)	C_{2h}	10.25, 1.34, 1.18	1351.8, 1355.3, 1601.8, 1701.2, 3309.3, 3335.2
N_2H_2(T)	C_2	11.72, 1.17, 1.16	783.5, 1079.8, 1088.7, 1509.7, 3363.1, 3384.5
N_2H_3	C_1	6.91, 1.04, 0.91	519.0, 710.8, 1154.5, 1293.8, 1496.0, 1668.8, 3485.1, 3549.2, 3687.8
N_2H_4	C_2	4.89, 0.82, 0.82	444.4, 829.7, 973.6, 1154.1, 1311.8, 1342.6, 1681.1, 1693.0, 3515.3, 3524.0, 3619.1, 3623.6
n-N_3H_5	C_1	1.37, 0.34, 0.30	334.5, 449.9, 493.8, 824.4, 850.8, 962.2, 1160.4, 1183.5, 1253.9, 1361.3, 1532.8, 1669.9, 1697.6, 3447.3, 3462.0, 3584.0, 3599.0, 3610.7
1,2-z-N_3H_5	C_1	1.35, 0.33, 0.30	241.6, 452.6, 482.2, 820.8, 936.0, 982.5, 1169.0, 1203.3, 1403.5, 1457.6, 1504.8, 1645.9, 1671.8, 3357.0, 3466.1, 3482.1, 3520.1, 3559.7
TS1	C_1	1.09, 0.19, 0.17	1900.0i, 25.3, 163.7, 244.1, 463.5, 660.1, 748.7, 844.3, 1163.5, 1175.4, 1363.4, 1443.2, 1557.7, 1667.4, 3380.8, 3520.4, 3561.1, 3661.9

11

TS2	C_1	1.11, 0.21, 0.18	1229.9i, 164.8, 191.2, 379.7, 542.4, 608.6, 673.5, 878.7, 1079.1, 1262.4, 1297.9, 1498.5, 1553.4, 1632.0, 3444.4, 3499.3, 3535.9, 3655.8
TS3	C_1	1.33, 0.25, 0.22	1409.4i, 232.8, 293.8, 415.5, 557.1, 644.0, 767.8, 812.5, 1221.3, 1346.0, 1515.4, 1569.9, 1690.0, 2568.3, 3503.0, 3522.2, 3619.1, 3627.1
TS4	C_1	1.19, 0.37, 0.31	1194.1i, 286.9, 543.7, 656.7, 847.9, 977.5, 985.2, 1127.7, 1196.8, 1418.5, 1483.3, 1547.7, 1607.4, 2262.6, 3432.7, 3469.5, 3490.7, 3574.8
TS5	C_1	1.37, 0.32, 0.28	1603.4i, 317.7, 362.8, 429.3, 811.7, 914.5, 976.4, 1136.5, 1243.4, 1392.0, 1472.9, 1533.3, 1680.1, 2751.3, 3439.8, 3452.8, 3594.0, 3622.4
TS6	C_1	1.48, 0.22, 0.20	870.5i, 184.6, 284.0, 478.1, 546.1, 632.8, 712.6, 987.4, 1178.4, 1459.8, 1540.9, 1545.8, 1705.5, 3325.9, 3469.7, 3476.7, 3566.4, 3624.4
TS7	C_1	1.18, 0.25, 0.21	1358.0i, 393.8, 453.4, 476.6, 722.7, 752.5, 769.0, 1178.8, 1460.0, 1557.1, 1559.4, 1642.2, 1657.3, 1749.3, 2375.8, 3156.2, 3610.3, 3706.0

Iminoammonium (NH$_3$NH) and H$_2$NNHN were previously shown to be important intermediates in hydrazine decomposition[10,12] and triazene (N$_3$H$_3$) rearrangements,[62] respectively. Three similar nitrenes on the N$_3$H$_5$ surface could potentially exist, namely NH$_2$NH$_2$NH, NH$_3$NNH$_2$, and NH$_3$NHNH, resulting from all possible intra-hydrogen transfers in the system. Nevertheless, only NH$_2$NH$_2$NH (referred to herein as 1,2-z-N$_3$H$_5$, Fig. 2) is unimolecularly connected to the entry channel, whereas rearrangements of n-N$_3$H$_5$ into NH$_3$NNH$_2$ and NH$_3$NHNH immediately lead to bimolecular products (e.g., via TS3 and TS4 in 1,2- and 1,3-NH$_3$ elimination reactions, respectively).
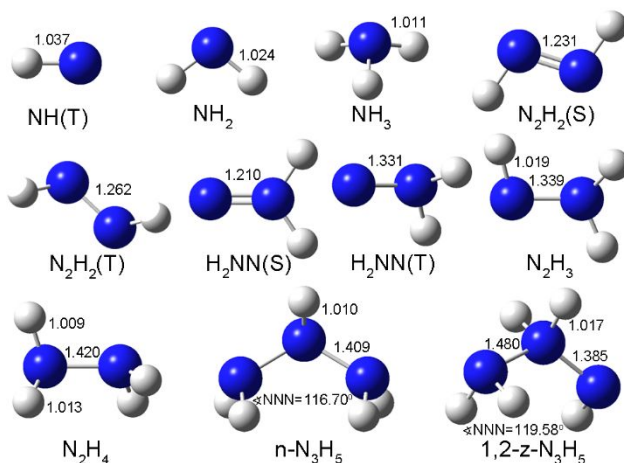
Figure 2. Geometric representation of species on the N_3H_5 PES optimized at the ωB97x-D3/6-311++G(3df,3pd) level of theory. Bond orders shown for illustration purpose only. Bond lengths are in Å and angles in degrees. Quantitative geometric data was added where it benefits the discussion; geometric coordinates for all species are available in the Supporting Information.

In addition to recombining to form n-N_3H_5, N_2H_3 + NH_2 can also react to directly form bimolecular products without going through the n-N_3H_5 well (see dashed lines in Fig. 1). On the singlet surface, disproportionation reactions proceed barrierlessly, forming either $N_2H_2(S)$ + NH_3 or $H_2NN(S)$ + NH_3. The triplet surface accommodates two hydrogen abstraction reactions via TS1 and TS2, forming N_2H_4 + NH(T), and $H_2NN(T)$ + NH_3, respectively, as well as a barrierless reaction forming $N_2H_2(T)$ + NH_3. The rate of the barrierless disproportionation reaction N_2H_3 + NH_2 $\leftrightarrow$ $H_2NN(S)$ + NH_3 (Reaction B2 in Table 2) was estimated by ascribing an activation energy of zero to the rate of the respective non-barrierless triplet reaction; in this estimation the rate of the latter was refitted, constraining its temperature exponent to be 0.5 to obey the collision theory. The rate of N_2H_3 + NH_2 $\leftrightarrow$ $N_2H_2(S)$ + NH_3 was adopted from Dean and Bozzelli[63] (Table 2). No rate was assigned for the N_2H_3 + NH_2 $\leftrightarrow$ $N_2H_2(T)$ + NH_3 reaction, which leads to the least stable product channel in the system.

We note that optimization efforts of $N_3H_5(T)$ at the ωB97x-D3/6-311++G(3df,3pd) level of theory resulted in conformers that could be further stabilized by rotating one of the dihedral angles in the molecule. However, all such rotations (of the two identical rotors) resulted in β-scission of the central hydrogen atom, yielding i-N_3H_4 + H. Since $N_3H_5(T)$ rapidly dissociates, intersystem crossing (ISC) behavior in the N_3H_5 PES is expected to be negligible. Additional ISC effects might play a role in the exit channels of this PES, and were not determined within the present framework.

13

Reactions R1 and R2 (Table 2) describe hydrogen abstractions between N_2H_3 and NH_2, where the abstracting radical is different in each reaction. Both transition states, TS1 and TS2 (Fig. 3) have similar angles between the atoms participating in the reaction, ∡NHN, of about 160-165°. The reactions are synchronous and resemble the reactants geometry in the exothermic direction: TS1 has a 16.0% N–H bond stretch fraction relative to N_2H_4, and a 31.5% stretch relative to NH_2, while TS2 has 10.3% and 40.8% stretches relative to N_2H_3 and NH_3, respectively. Bond stretch fractions throughout the discussion are defined as $(r_{TS} - r_{stable}) / r_{stable}$, where r_{stable} and r_{TS} are the relevant bond lengths in the stable species (either reactant or product, where this bond exists) and the TS, respectively. In the exothermic direction, Reaction R2 has an exceptionally low energy barrier of just 4.8 kJ mol^{-1} (Fig. 1). It could be explained by the hydrogen bond formed between the nitrogen atom in the abstracting NH_2 group and one of the hydrogen atoms in N_2H_3, stabilizing this saddle point (Fig. 4).

The transition state of Reaction R3, leading to $H_2NN(S)$ + NH_3 from the n-N_3H_5 isomer via a 1,2-NH_3 elimination route, is asynchronous, characterized by relatively large stretches in both N–N (46.0%) and terminal N–H (36.6%) bonds. These relatively large stretches explain the high E0 of TS3, 128.3 and 183.9 kJ mol^{-1} above the $H_2NN(S)$ + NH_3 and n-N_3H_5 wells, respectively. The N–H bond stretch fraction in the intermediate nitrogen site, however, is significantly lower (6.8%). The ∡NNN backbone angle is smaller than in the n-N_3H_5 isomer (108.79° vs. 116.70°). Indeed, a Mulliken electronic population analysis[64] showed that the reacting NH_2 group (which leaves as NH_3) and the non-reacting NH_2 group have net formal charges of -0.33 and +0.24, respectively, while each of these groups has a net formal charge of -0.03 in the n-N_3H_5 isomer. The resulting electrostatic attraction forces cause the backbone angle to be smaller than in the isomer.

14

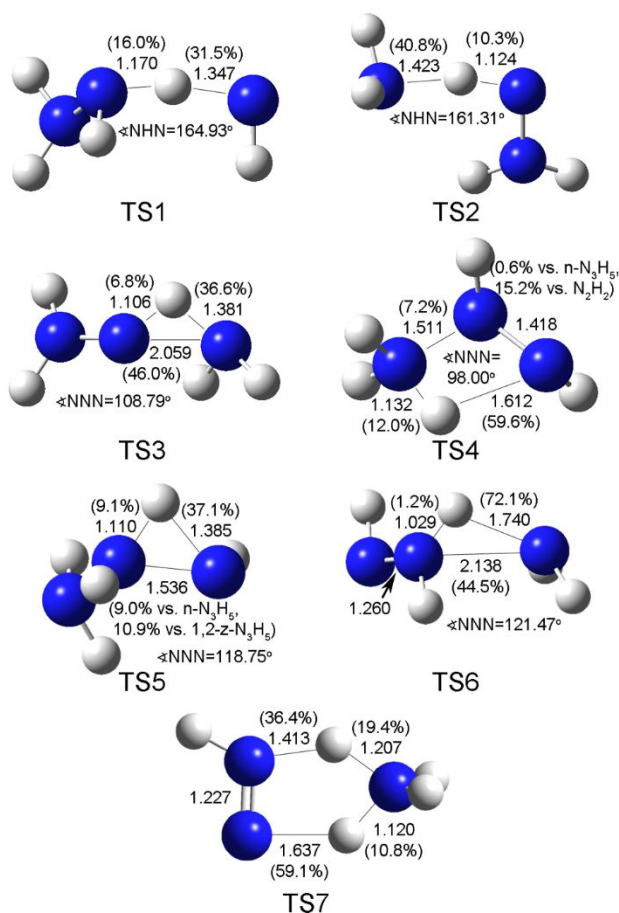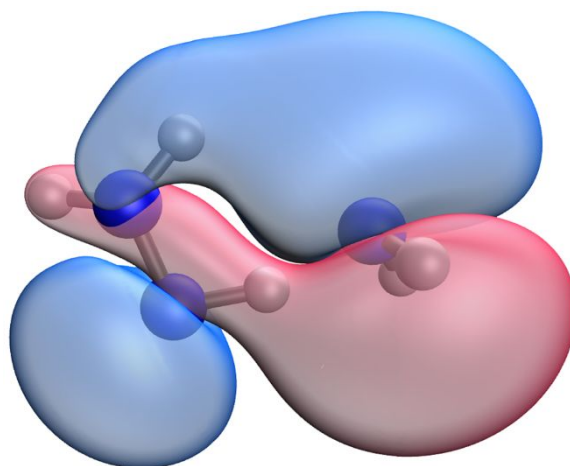**Figure 3.** Geometric representation of transition states on the N_3H_5 PES optimized at the ωB97x-D3/6-311++G(3df,3pd) level of theory. Bond lengths are in Å and angles in degrees. Numbers in parentheses indicate the bond stretch fraction relative to the respective stable species. Quantitative geometric data was added where it benefits the discussion; geometric coordinates for all transition states are available in the Supporting Information.

TS4 is the saddle point of a 1,3-NH_3 elimination reaction of n-N_3H_5. While the cyclic group in TS3 (describing a 1,2-NH_3 elimination reaction) is -N-H-N-, the geometry of TS4 involves a very strained four-membered ring group, -N-H-N-N-, distorting the molecule backbone. The formed ∢NNN angle in TS4 is significantly smaller than in n-N_3H_5, only 98.00° vs. 116.70°. The N–N bond not directly participating in the reaction (with a bond length of 1.418 Å, Fig. 3) is stretched relative to both reactant and product, in accordance with the high strain induced by the cyclic transition: slightly vs. n-N_3H_5 (0.6%), and more significantly vs. N_2H_2(S) (15.2%). As expected from the energetics of the reaction, the length of this bond is more similar to the respective value in

15

n-N_3H_5. This transition is asynchronous, since the hydrogen transfer has significantly progressed (having a 12.0% stretch relative to ammonia and a 59.6% stretch relative to n-N_3H_5), while the N–N scission has only started (7.2% stretch relative to n-N_3H_5).

Figure 4. Highest alpha-electron occupied molecular orbital (MO 12) in the triplet saddle point TS2, computed at the ωB97x-D3/6-311++G(3df,3pd) level of theory.

The isomerization pathway via TS5 involves an internal hydrogen transfer between two adjacent nitrogen atoms in n-N_3H_5; yet unlike TS3, here the intermediate nitrogen atom is a hydrogen acceptor instead of a donor, resulting in a saddle point raised 82.3 kJ mol^{-1} above TS3. In contrast to TS3, the N–N bond is stretched significantly less (9.0% vs. n-N_3H_5 and 10.9% vs. 1,2-z-N_3H_5 compared to 46.0% in TS3) and does not result in scission. The ∡NNN backbone angle is also intermediate relative to the reacting isomers, and slightly closer to the angle in the higher energy nitrene isomer. The distances of the migrating hydrogen with respect to both nitrogen atoms are markedly uneven (9.1% vs. 1,2-z-N_3H_5 and 37.1% vs. n-N_3H_5); this criterion too suggests a greater resemblance of the saddle point geometry to the nitrene isomer, in accordance with the reaction energetics.

An additional 1,2-NH_3 elimination reaction in this system passes through TS6. Similarly to TS3 which belongs to the same reaction family, TS6 is also asynchronous with significant bond stretch

16

fractions with regard to 1,2-z-N_3H_5 (44.5% N–N stretch) as well as NH_3 (a 72.1% N–H stretch). The

large N–H bond stretch fraction is particularly peculiar when compared to the minor N–H bond

stretch fraction of the intermediate nitrogen site (only 1.2%), as well as to the respective stretch

in TS3 (only 36.6%). Moreover, the N–N bond not directly participating in the reaction is closer in

length to the N_2H_2(S) product (1.260 Å in TS6 vs. 1.231 Å in N_2H_2(S) and 1.385 Å in 1,2-z-N_3H_5).

Finally, the formed ∢NNN backbone angle is slightly larger than in the reacting isomer (121.47°

vs. 119.58°), unlike the TS3 case. A Mulliken electronic population analysis of TS6 shows that the

reacting NH_2 group and the non-reacting NH group have net formal charges of -0.45 and -0.19,

respectively. The resulting electrostatic repulsion forces cause the backbone angle to be wider

than in the isomer. It is noted that these groups have net formal charges of +0.12 and -0.43,

respectively, in 1,2-z-N_3H_5. Calculated high-pressure-limit rates for the above reactions (R1–R6),

as well as estimated rates for barrierless reactions on the N_3H_5 diagram are given in Table 2.

Reaction R7 catalyzes the H_2NN(S) to N_2H_2(S) transformation using ammonia via a five

member ring TS. This simultaneous hydrogen transfer TS is asynchronous. The bond lengths of

the reacting hydrogens and their neighboring nitrogen atoms suggests an early TS, resembling

H_2NN(S) + NH_3. Nevertheless, the N–N bond length (1.227 Å) is closer to the respective bond in

N_2H_3(S) (1.231 Å) rather than to the bond in H_2NN(S) (1.210 Å).

Table 2. High-Pressure-Limit Rates of Elementary Reactions on the N_3H_5 PES[a]

no.[b]	reaction	A[c]	n	Ea (kJ mol^{-1})	source[d]
R1	$N_2H_4 + NH$(T) ↔ $N_2H_3 + NH_2$	6.09E+01	3.61	24.3	pw
R2	$N_2H_3 + NH_2$ ↔ H_2NN(T) + NH_3	3.10E+00	3.43	-8.2	pw
R3	n-N_3H_5 ↔ H_2NN(S) + NH_3	1.04E+10	1.14	177.1	pw
R4	n-N_3H_5 ↔ N_2H_2(S) + NH_3	1.40E+09	0.92	213.3	pw
R5	n-N_3H_5 ↔ 1,2-z-N_3H_5	7.94E+09	0.85	103.9	pw
R6	1,2-z-N_3H_5 ↔ N_2H_2(S) + NH_3	6.57E+11	0.57	41.2	pw
R7	H_2NN(S) + NH_3 ↔ N_2H_2(S) + NH_3	2.07E-01	3.64	31.1	pw
B1	$N_2H_3 + NH_2$ ↔ n-N_3H_5	5.02E+14	-0.43	0.2	ref 61

17

B2	$N_2H_3 + NH_2 \leftrightarrow H_2NN(S) + NH_3$	3.00E+10	0.50	0	est., pw
B3	$N_2H_3 + NH_2 \leftrightarrow N_2H_2(S) + NH_3$	9.20E+05	1.94	4.8	ref 65

[a] Parameters are for the modified Arrhenius expression, $k = A\, T^n \exp(-E_a/[RT])$, in the 500–3000 K temperature range; the rate of Reaction B1 is valid in the 200–2500 K temperature range.

[b] The R notations refer to reactions as discussed in the text, numbers match the transition states in Fig. 3. The B notations refer to barrierless reactions.

[c] Units are s^{-1}, or $cm^3\ mol^{-1}\ s^{-1}$ for first- or second-order reactions in the forward direction, respectively.

[d] pw – calculated in the present work (see text); est. – estimated (see text).

It is noted that the N_2H_3 radical has strong coupling between large amplitude fluxional inversion of the amine group and a hindered rotor mode (Fig. S3). This behavior, characterized by discontinuities in the potential scan curve due to an abrupt geometry change in the nitrogen backbone, is known to occur in similar systems.[16] A local maximum of ~80 kJ mol^{-1}, reached before the inversion point, and a global maximum of ~100 kJ mol^{-1} suggest that this mode is significantly hindered. It was therefore not considered as a rotor in any of the calculations in the present work. Although thermodynamic properties of N_2H_3 are known,[66,67] the authors are not aware of a literature discussion of its 1-D hindered rotor.

The rate of Reaction R1 (Table 2) was previously estimated by Konnov and De Ruyck[9] based on experimental and theoretical values for other $NH(T) + RH \leftrightarrow NH_2 + R$ hydrogen abstraction reactions, implementing an activation energy correction based on the Evans-Polani correlation. The present calculation and the previous estimation were found to be similar at ~1250 K, yet the Konnov and De Ruyck rate has a somewhat lower temperature dependence despite efforts to adjust its activation energy in that study (Fig. 5). Overall, the disagreement between these rates is acceptable, considering that one of the rates is an estimate.
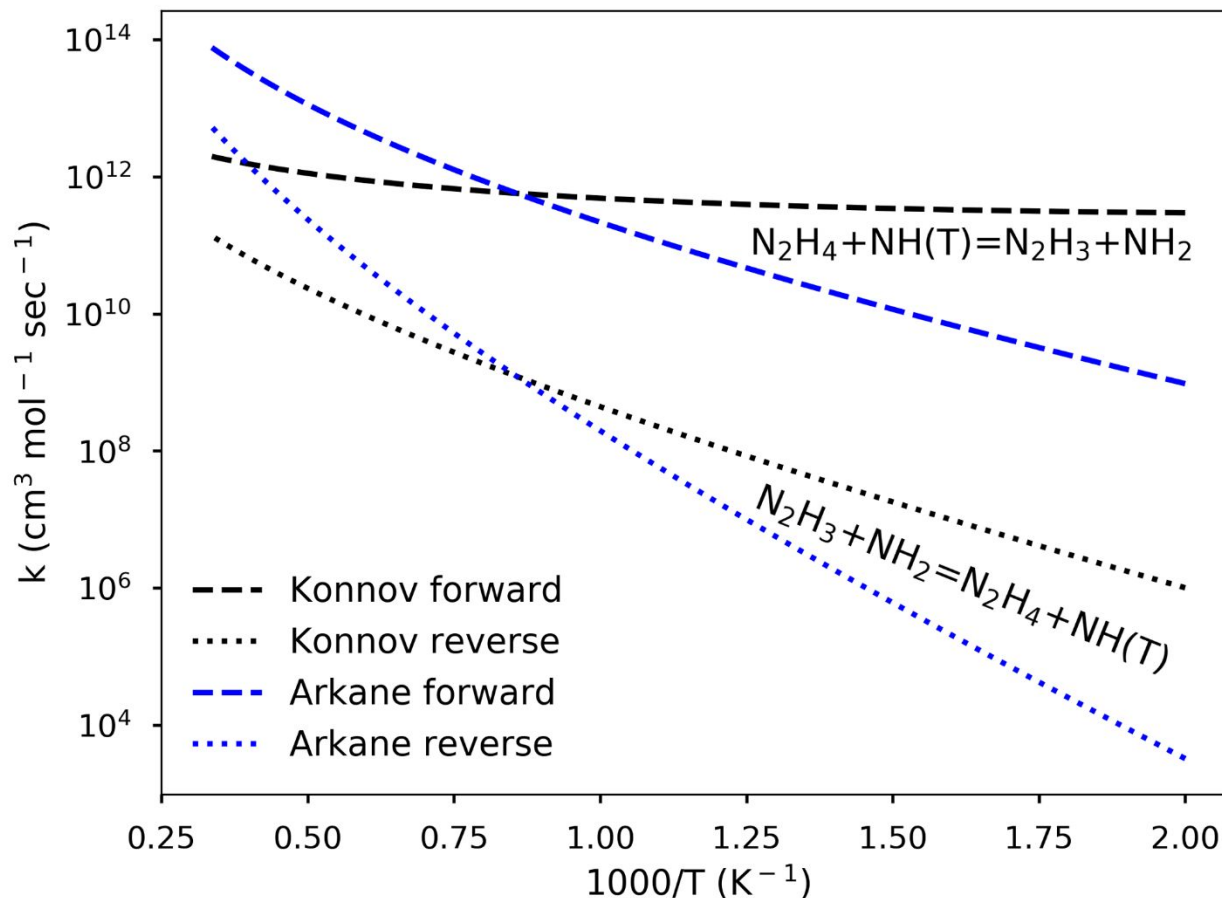
18

Figure 5. Rate comparisons of Reaction R1 (forward) and R-1 (reverse) between the present work calculation using Arkane and the rate estimated and reported by Konnov and De Ruyck.[9] Thermodynamic data from Curran et al.[67] was used to compute reverse rates.

As mentioned above, while $N_2H_2(S) + NH_3$ is more stable, the formation route of $H_2NN(S) + NH_3$ has a lower barrier (TS3, Fig. 1). Indeed, the rate of the well-skipping reaction $N_2H_3 + NH_2 \leftrightarrow H_2NN(S) + NH_3$ is orders of magnitude faster than the respective rate of the competing reaction forming $N_2H_2(S)$ throughout the entire temperature and pressure ranges considered here (Fig. 6 a, b). The RRK (Rice-Ramsperger-Kassel) estimation by Dean and Bozzelli[63] for $N_2H_3 + NH_2 \leftrightarrow H_2NN(S) +$ by a well-skipping reaction via $n-N_3H_5$ is shown here to over-estimate the respective calculated rates by about two orders of magnitude (Fig. 6 a), because Dean and Bozzelli assumed TS3 had a lower barrier. Due to higher collisional stabilization of $n-N_3H_5$, the $k(T,P)$ for $N_2H_3 + NH_2 \leftrightarrow H_2NN(S) + NH_3$ decreases at high pressures. Interestingly, this rate coefficient is not monotonic

19

with temperature at low pressures (Fig. 6 a) because this reaction over TS3 is competing with

dissociation back to the reactants.

Each of the product channels on this PES could also be formed via bimolecular non-pressure-

dependent routes from N_2H_3 + NH_2. While the direct route forming $N_2H_2(S)$ is faster than the

respective well skipping reaction, the major formation route of $H_2NN(S)$ is the well skipping

reaction at low pressures and temperatures and it is not negligible at the other studied conditions

(Fig 6 a, b). Accounting for both unimolecular and bimolecular pathways, $H_2NN(S)$ formation is

favorable over $H_2N_2(S)$ in this PES, contrary to a past kinetic stability estimation.[17] Since rates for

both direct routes were estimated (in the present work and by Dean and Bozzelli), further work

to determine these values with lower uncertainties is desired.

20
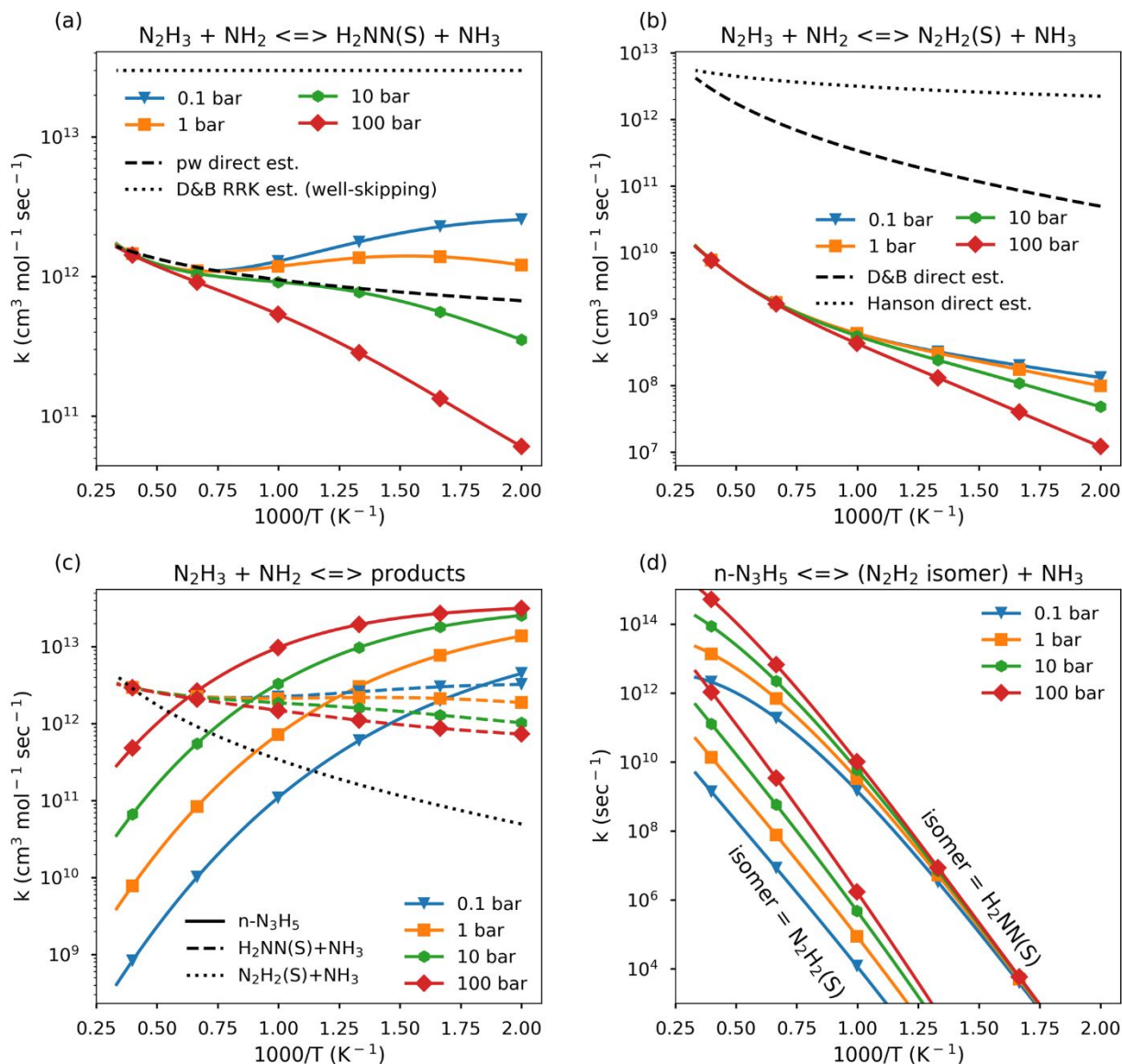
Figure 6. Rate comparisons of selected reactions on the N_3H_5 PES. 'D&B' in the legend refers to the book chapter by Dean and Bozzelli from 2000,[63] and 'Hanson' refers to a N/H/O rate constants review by Hanson and Salimian from 1984.[68] Present work is denoted as 'pw'. In (c), line types refer to the product/s, while the color refers to the pressure; the pressure-dependence of the $N_2H_2(S) + NH_3$ formation rate is negligible, while formation rates of $H_2NN(S) + NH_3$ include both pressure-dependent and direct routes; the updated Dean and Bozzelli rate for $N_2H_2(S) + NH_3$ is shown.

While 1,2-z-N_3H_5 formation in this network is negligible (rates not shown), n-N_3H_5 formation is significant due to the relatively high barriers surrounding this isomer (Fig. 1). As expected, n-N_3H_5 formation becomes more significant at high pressures due to collisional stabilization (Fig. 6

21

c). It is also the major product in the network below a pressure-dependent temperature

threshold: at 0.1, 1, 10, 25, and 100 bar this threshold is about 550, 800, 1150, 1250, and 1600 K,

respectively. The n-N_3H_5 isomer decomposes either while still excited at relatively low pressures

if the temperature is high enough, forming preferably $H_2NN(S)$ and NH_3 (Fig. 6 d), or after

stabilization via hydrogen abstraction reactions mediated by the radical pool (mostly H, NH_2, and

N_2H_3 in hydrazine decomposition systems). All relevant pressure-dependent rate coefficients for

this PES are available in the Supporting Information.
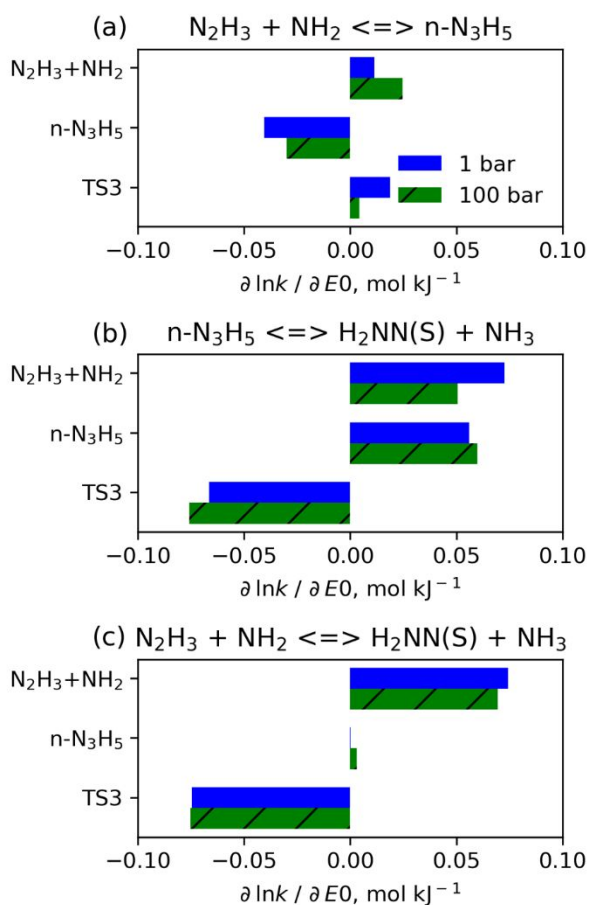
Figure 7. Normalized sensitivity coefficients to ZPE-corrected energies of $N_2H_3 + NH_2$, n-N_3H_5, and TS3 for selected pressure-dependent rates on the N_3H_5 potential at 1 and 100 bar and at 1500 K.

A sensitivity analysis of pressure-dependent rates on the N_3H_5 PES was conducted,

implementing the chemically-significant eigenstate approach.[69,70] This approach is more accurate

22

than the MSC approximation, yet less robust, i.e., often fails to converge for relatively large systems. Therefore, only the $N_2H_3 + NH_2$, n-N_3H_5, and $H_2NN(S) + NH_3$ species on the N_3H_5 PES were considered for the sensitivity analysis. Results for three selected pressure-dependent reactions, describing $H_2NN(S) + NH_3$ formation either via formation of the n-N_3H_5 intermediate or skipping the isomer well are shown (Fig. 7).

The sensitivity coefficients for the $N_2H_3 + NH_2 \leftrightarrow$ n-N_3H_5 reaction (Fig. 7 a) suggest that this reaction is in the pressure-dependent "fall-off" region at 1 bar and 1500 K. Increasing E0 of either the $N_2H_3 + NH_2$ or the n-N_3H_5 wells changes the density of states around the entry well, increasing or decreasing the rate, respectively. The sensitivity coefficients for n-N_3H_5 are lower at the higher pressure, since at higher pressures the excited complex lifetime is much shorter, leading to less significant competition from the route via TS3. The $N_2H_3 + NH_2$ well has a higher sensitivity coefficient at the higher pressure, since the leak rate through the submerged barrier TS3 forming $H_2NN(S) + NH_3$ is much lower at this condition, and a change in the entrance well E0 has a larger relative impact.

The n-$N_3H_5 \leftrightarrow H_2NN(S) + NH_3$ reaction rate has a complex dependency on E0 of the adduct, the $N_2H_3 + NH_2$ asymptote, and TS3 (Fig. 7 b). Perturbing the n-N_3H_5 well or the TS3 saddle point results in the expected behavior of the system: increasing E0 of n-N_3H_5 or TS3 increases or decreases the rate, respectively. The system is slightly more sensitive to these parameters at the higher pressure (unlike the previous case) since this is a thermally activated reaction. Increasing E0 of the $N_2H_3 + NH_2$ channel results in a slower reverse rate (n-$N_3H_5 \leftrightarrow N_2H_3 + NH_2$), changing the branching ratio more in favor of the $H_2NN(S) + NH_3$ products. As the pressure increases, the

23

reverse reaction becomes even less favorable, as reflected in the respective sensitivity coefficients at the different pressures.

The rate coefficient of the well-skipping reaction $N_2H_3 + NH_2 \leftrightarrow H_2NN(S) + NH_3$ (Fig 7 c) is sensitive to the energies of the entry channel and transition state, as expected. Increasing E0 of the entry channel broadens the energy gap between this well and TS3, resulting in a higher rate, while increasing E0 of TS3 has the opposite effect. This rate coefficient is relatively insensitive to the energy of $n-N_3H_5$.

The pressure-dependent rate sensitivity analysis allows one to assess the effects of uncertainties in this system. All sensitivity coefficients had values below 0.1 mol kJ^{-1}. The sensitivity coefficients of the important $N_2H_3 + NH_2 \leftrightarrow n-N_3H_5$ reaction, which has a significant flux in this system (Fig. 6 c), were below 0.05 mol kJ^{-1}. Therefore, if we can determine the E0's to within about 10 kJ mol^{-1}, the rate coefficient uncertainty due to uncertainties in energies will be less than a factor of 2.

To assess the uncertainties due to estimations of barrierless reaction rates, we conducted a sensitivity analysis for the pressure-dependent rate coefficient of $N_2H_3 + NH_2 \leftrightarrow H_2NN(S) + NH_3$ by perturbing the PES entry channel, $N_2H_3 + NH_2 \leftrightarrow n-N_3H_5$. At 1, 15, and 80 bar these normalized (dimensionless) sensitivity coefficients were 0.06, 0.10, and 0.14, respectively. At 15 bar, for example, perturbing the rate coefficient of the barrierless entry channel by factors of 1.05 and 1.50 resulted in 0.5% or 3.4% change, respectively, in the k(T,P) of $N_2H_3 + NH_2 \leftrightarrow H_2NN(S) + NH_3$.

We note that at high temperatures well merging could add additional uncertainties to the calculated rates. For example, at high enough temperatures the $1,2-z-N_3H_5$ isomer could merge with the $N_2H_2(S) + NH_3$ product well. Calculating the pressure-dependent rate of the well-skipping

24

reaction $N_2H_2 + NH_2 \leftrightarrow N_2H_2(S) + NH_3$ after forcing the above wells to merge has no significant

effect at 1000 K, yet reduces the rate by a factor of 1.25 at 3000 K.

3.2. The N_4H_6 system

High N_2H_3 concentration may lead to high fluxes on the N_4H_6 potential. The N_3H_5 and N_4H_6

systems are related since $H_2NN(S)$, a major product of the N_3H_5 PES, could react with hydrazine

which has a high concentration at early times in the system. The $N_2H_4 + H_2NN(S)$ well, in turn, is

one of the entry channels on the potential. Nevertheless, it is noted that $H_2NN(S)$ may have more

important formation routes such as N_2H_3 disproportionation reactions. An additional entry

channel on this potential is $N_2H_3 + N_2H_3$. These two channels are inter-convertible bimolecularly

(Fig. 8).

Various non-P-dependent dissociation products could be formed from the two reacting N_2H_3

radicals on both the singlet and triplet surfaces, of which the $N_2H_4 + N_2H_2(S)$ well is particularly

stable. For simplicity, the highly energetic wells $NH_3NH + H_2NN(S)$, $NH_3NH + H_2NN(T)$, and NH_3NH

$+ N_2H_2(T)$ with energies (on the scale selected for Fig. 8) of 183.1, 247.5, and 259.6 kJ mol^{-1},

respectively, are not shown. Two additional highly energetic product wells of the barrierless

reactions $1,2$-z-$N_4H_6 \leftrightarrow NHNH_2NH + NH_2$ and $2,3$-z-$N_4H_6 \leftrightarrow NH_2NH_2N + NH_2$ with energies of 682.7

and 706.4 kJ mol^{-1}, respectively, were excluded. Geometric representations of relevant species

and saddle points are given in Figs. 9, 10, respectively. Table S2 lists point groups, rotational

constants, and unscaled vibrational frequencies for all relevant species and transition states.

The high pressure limit rate for the entry channel $N_2H_3 + N_2H_3 \leftrightarrow n\text{-}N_4H_6$ (Reaction B4, Table

3) was estimated using RMG[30] based on its radical recombination reaction family

("R_Recombination"). This rate was estimated to be slower by a factor of 2 with respect to the

25

estimate of Zhang et al. for the similar recombination Reaction B1 (Table 2).[61] The high pressure

limit rates for the exit channels n-$N_4H_6 \leftrightarrow$ n-N_3H_4 + NH_2, 1,2-z-$N_4H_6 \leftrightarrow NHNH_2NH$ + NH_2, and 2,3-z-

$N_4H_6 \leftrightarrow iN_3H_4$ + NH_2 (Reactions B5–B7) were estimated similarly using the radical recombination

family in RMG. All high-pressure-limit rates are given in Table 3. The respective microcanonical

rates were calculated by Arkane using an inverse Laplace transform.

The pressure-dependent network on the singlet surface potential has three stable isomers, n-

N_4H_6 (tetrazane), 1,2-z-N_4H_6, and 2,3-z-N_4H_6 (Figs. 8, 9). Similar to the N_3H_5 case, additional

zwitterionic isomers could theoretically be thought of, yet only the two isomers listed above and

illustrated in Fig. 9 were found to be connected to the network by isomerizations. Most of the

saddle points on the N_4H_6 potential are located within a relatively narrow energy range of 56.4–

73.3 kJ mol^{-1} above N_2H_4 + H_2NN(S) (Fig. 8), making the various transitions quite competitive. The

two exceptions are TS12 and TS15 with relatively high energies, which are expected to

significantly inhibit the flux through the respective channels.

Consequently, an interesting phenomenon emerges where a different entry channel would

favor a different final product. A chemically-activated complex formed by a N_2H_4 + H_2NN(S)

collision could form n-N_4H_6 via TS9, or 2,3-z-N_4H_6 via TS10. The energized n-N_4H_6 is likely to either

be collisionally stabilized, or rapidly dissociate to form two N_2H_3 radicals, depending on the

pressure and temperature. If 2,3-z-N_4H_6 is formed via TS10, it will rapidly dissociate to form either

i-N_3H_4 + NH_2 or NH_2NNH + NH_3.

On the other hand, an excited complex formed by a N_2H_3 + N_2H_3 collision will most likely be

collisionally stabilized, forming n-N_4H_6, or dissociate back to N_2H_3 + N_2H_3. The alternative

pathways for continued reaction via TS9 or TS11, or the barrierless dissociation to n-N_3H_4 + NH_2

26

are all significantly uphill compared to the $N_2H_3 + N_2H_3$ entry channel. Note that the $N_2H_3 + N_2H_3$

and $N_2H_4 + H_2NN(S)$ entry channels are interconvertible bimolecularly via a relatively low energy

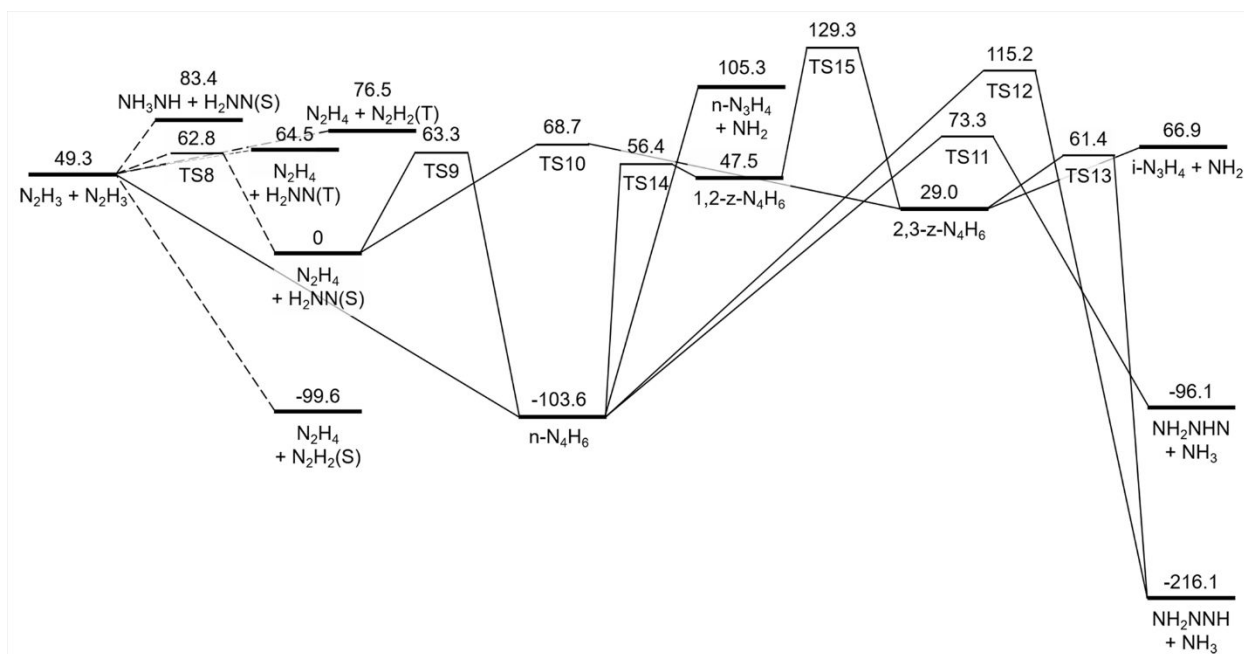saddle point, TS8, but $N_2H_3 + N_2H_3$ is more likely to undergo barrierless disproportionation to

$N_2H_3 + N_2H_2(S)$.

Figure 8. Reaction path diagram for the N_4H_6 potential. Dashed lines represent non-pressure-dependent pathways. (S) and (T) represent singlet or triplet multiplicities, respectively. Energies are in kJ mol^{-1}, and scaled relative to the $N_2H_4 + H_2NN(S)$ entry channel, which was set at zero.

TS8 is the saddle point of the $N_2H_3 + N_2H_3$ disproportionation reaction forming $N_2H_4 +$

$H_2NN(S)$. It is an early and synchronous transition state, as expected from the reactants and

products energetics. It is noted that this reaction was found to be intrinsically different from a

similar reaction on the N_3H_5 potential, $N_2H_3 + NH_2 \leftrightarrow H_2NN(S) + NH_3$ (Reaction B2, Table 2),
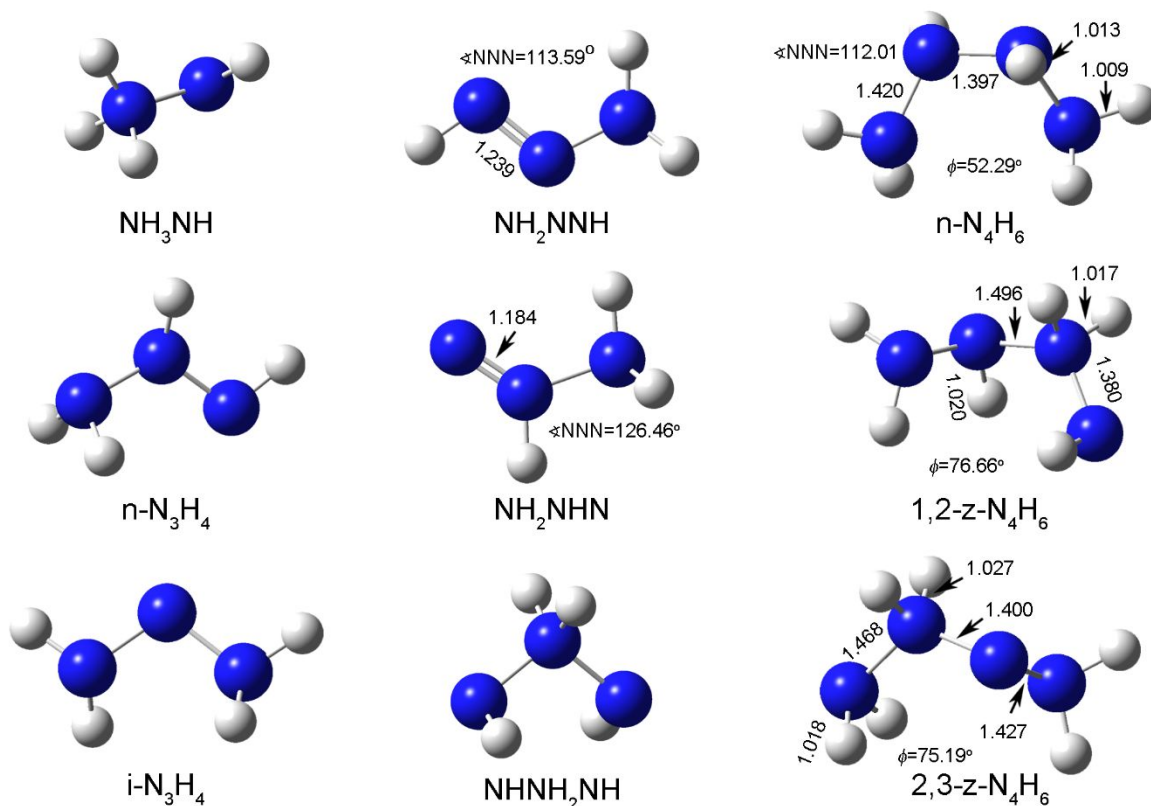
where the latter was determined to be barrierless.

Figure 9. Geometric representation of species on the N_4H_6 PES optimized at the ωB97x-D3/6-311++G(3df,3pd) level of theory. Species already given in Fig. 2 were not reproduced here. Bond orders shown for illustration purpose only. Bond lengths are in Å and angles in degrees. ϕ is the dihedral angle between the four nitrogen backbone atoms. Quantitative geometric data was added where it benefits the discussion; geometric coordinates for all species are available in the Supporting Information.

TS9, a saddle point of a nitrene insertion into an N–N bond, is asynchronous. Most interestingly, the N–N bond length in the substructure originated from N_2H_4 is shorter than the respective bond lengths in both the reactant N_2H_4 and the product n-N_4H_6 (1.379 vs. 1.420 and 1.397 Å, respectively). TS8 and TS9 are geometrically and energetically similar (Figs. 8, 10). The major difference between these geometries is the orientation of the terminal hydrogens not directly participating in the reaction, which causes the complex to either recombine or fall apart due to electrostatic forces.
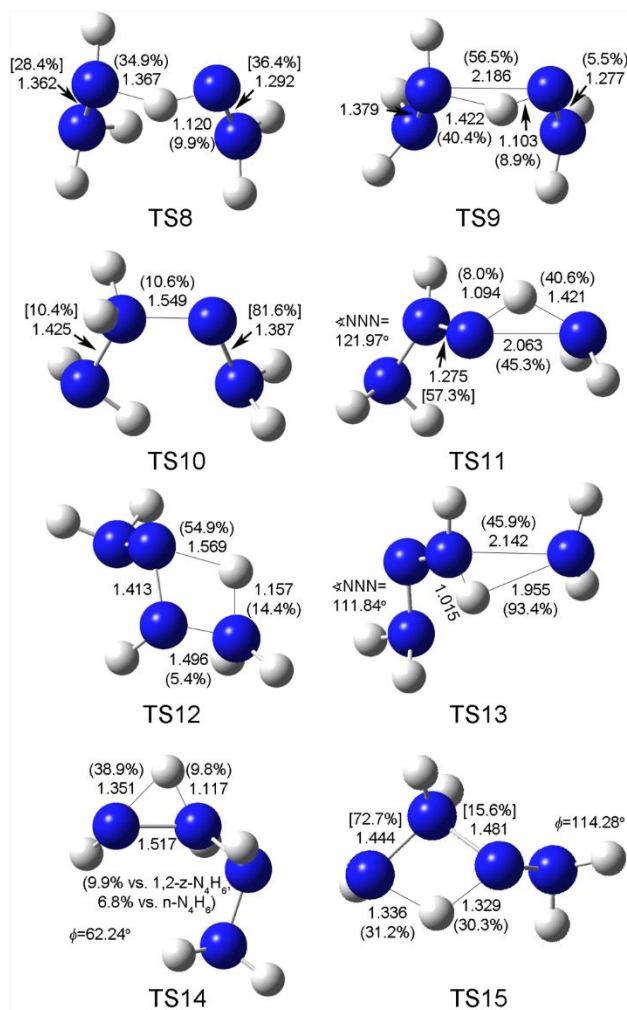
Figure 10. Geometric representation of transition states on the N_4H_6 PES optimized at the ωB97x-D3/6-311++G(3df,3pd) level of theory. Bond lengths are in Å and angles in degrees. Numbers in parentheses indicate the bond stretch fraction relative to the respective stable species. Numbers in brackets indicate the relative bond stretch fraction out of the total change between the respective reactant and product in the direction specified in Table 3. ϕ is the dihedral angle between the four nitrogen backbone atoms. Quantitative geometric data was added where it benefits the discussion; geometric coordinates for all transition states are available in the Supporting Information.

The addition reaction $N_2H_4 + H_2NN(S) \leftrightarrow 2,3\text{-}z\text{-}N_4H_6$ passes through TS10. This TS has a similar geometry to the product except the central N–N bond has stretched significantly. It is an asynchronous transition in which the N–N bond length of the $H_2NN(S)$ reactant stretches considerably (81.6% stretch fraction) before reaching the saddle point while the N–N bond length of the N_2H_4 reactant hardly stretches (10.4% stretch fraction). Relative bond stretch fractions

29

throughout the discussion are defined as $(r_{TS} - r_{reactant}) / (r_{product} - r_{reactant})$, where $r_{reactant}$, $r_{product}$,

and r_{TS} are the relevant bond lengths in the reactant, product, and the TS, respectively.

Two reactions of the 1,2-NH$_3$ elimination family on this potential pass through transition states

TS11 and TS13. In both cases, the ∢NNN backbone angles of the forming products in the TS are

close to the values of the stable NH$_2$NHN and NH$_2$NNH products, respectively. Both are

asynchronous, primarily characterized by a highly stretched N–N bond of the leaving NH$_2$ group

(45.3% and 93.4%, respectively), and a low stretch of the N–H bond to be ruptured. In fact, the

respective N–H bond in TS13 is shorter than in the reactant and overall the geometry and

energies indicate that NH$_2$ was nearly dissociated but grabbed an H atom as it departed. Methods

developed for roaming reactions[71] may be helpful for better evaluating this rate.

A 1,3-NH$_3$ elimination reaction on this surface, n-N$_4$H$_6$ $\leftrightarrow$ NH$_2$NNH + NH$_3$, has a strained four-

membered ring transition geometry, TS12. This transition state is also asynchronous with the

central N–N bond stretched relative to both reactants and products, and a small ∢NNN ring angle

of 98.78°, all of which are similar characteristics to TS4 (Fig. 3).

TS14 and TS15 are saddle points of isomerization reactions on this surface: n-N$_4$H$_6$ $\leftrightarrow$ 1,2-z-

N$_4$H$_6$ and 1,2-z-N$_4$H$_6$ $\leftrightarrow$ 2,3-z-N$_4$H$_6$. Note that no direct reaction was identified between n-N$_4$H$_6$

and 2,3-z-N$_4$H$_6$. Exhaustive searches for such saddle point always lead to dissociation of the

complex into N$_2$H$_4$ and H$_2$NN(S), as this pathway resembles the geometry of TS9 (Fig. 10). The

transition geometry of TS14 is synchronous and late as expected from the reaction energetics.

Facilitating the internal hydrogen transfer in this reaction causes the N–N bond over which this

transfer occurs to stretch relative to both relevant isomers. The geometry of TS15, on the other

hand, is asynchronous; although the hydrogen stretches nearly evenly on both sides (30.3% and

30

31.2%), the outer N–N bond stretches considerably (72.7% relative bond stretch fraction) while

the internal N–N bond stretches slightly (15.6% relative bond stretch fraction).

Table 3. High-Pressure-Limit Rates of Elementary Reactions on the N_4H_6 PES[a]

no.[b]	reaction	A[c]	n	Ea (kJ mol^{-1})	source[d]
R8	$N_2H_3 + N_2H_3 \leftrightarrow N_2H_4 + H_2NN(S)$	1.11E-01	3.21	-1.5	pw
R9	$N_2H_4 + H_2NN(S) \leftrightarrow n-N_4H_6$	4.73E-01	3.55	50.6	pw
R10	$N_2H_4 + H_2NN(S) \leftrightarrow 2,3-z-N_4H_6$	2.29E+00	2.96	55.4	pw
R11	$n-N_4H_6 \leftrightarrow NH_2NHN + NH_3$	3.00E+12	0.83	178.7	pw
R12	$n-N_4H_6 \leftrightarrow NH_2NNH + NH_3$	7.70E+10	0.84	214.1	pw
R13	$2,3-z-N_4H_6 \leftrightarrow NH_2NNH + NH_3$	4.03E+13	0.26	38.7	pw
R14	$n-N_4H_6 \leftrightarrow 1,2-z-N_4H_6$	7.90E+11	0.59	158.6	pw
R15	$1,2-z-N_4H_6 \leftrightarrow 2,3-z-N_4H_6$	1.74E+10	0.91	74.4	pw
B4	$N_2H_3 + N_2H_3 \leftrightarrow n-N_4H_6$	2.51E+14	-0.43	0.2	est., pw
B5	$n-N_3H_4 + NH_2 \leftrightarrow n-N_4H_6$	5.02E+14	-0.43	0.2	est., pw
B6	$NHNH_2NH + NH_2 \leftrightarrow 1,2-z-N_4H_6$	5.02E+14	-0.43	0.2	est., pw
B7	$i-N_3H_4 + NH_2 \leftrightarrow 2,3-z-N_4H_6$	1.17E+16	-1.26	2.8	est., pw
B8	$N_2H_3 + N_2H_3 \leftrightarrow N_2H_4 + N_2H_2(S)$	1.20E+13	0	0	ref [9]

[a] Parameters are for the Modified Arrhenius Expression, k = A Tn exp(-Ea/[RT]), in the 500–3000 K Temperature Range.

[b] The R notations refer to reactions as discussed in the text, numbers match the transition states in Fig. 10. The B notations refer to barrierless reactions.

[c] Units are s[-1], or cm[3] mol^{-1} s^{-1} for first- or second-order reactions in the forward direction, respectively.

[d] pw – calculated in the present work (see text); est. – estimated (see text).

The n-N_4H_6 formation rate is higher when entering from the $N_2H_3 + N_2H_3$ channel, compared to N_2H_4 +

$H_2NN(S)$ (Fig. 11), due to the relatively high energy barrier in the later (Fig. 8). As expected, more n-N_4H_6

is formed with respect to both entry channels as the pressure increases. The rate coefficient of the

estimated Reaction B4 (Table 3) is within a factor of 2 from the rate of the calculated and comparable

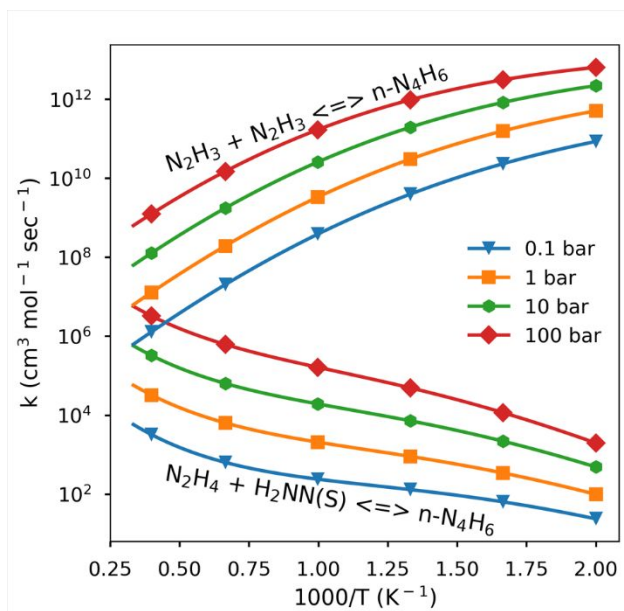Reaction B1 (Table 2) forming n-N_3H_5 for all studied conditions (Fig. 6 c, Fig. 11).

Figure 11. Rate coefficient comparison of n-N_4H_6 formation from each of the entry channels as a function of temperature and pressure.

Rate coefficient comparison starting from each of the entry channels on the N_4H_6 potential suggests a single dominant product channel, $N_2H_4 + N_2H_2$(S), though at high pressures n-N_4H_6 formation is comparable; $N_2H_4 + H_2NN$(S) would preferably form $N_2H_3 + N_2H_3$ (Fig. 12 a), which in turn mostly yield $N_2H_4 + N_2H_2$(S) (Fig. 12 b). The tendency of N_2H_3 radicals to react via a disproportionation route rather than recombine to form n-N_4H_6 was previously observed experimentally at 298 K and 1 bar, and a branching ratio of four was determined.[19] Our calculated rate for the recombination Reaction R9 at these conditions (3.0E+12 cm^3 mol^{-1} sec^{-1}) is a factor of 3.3 lower than the disproportionation rate (Reaction R8) estimated by Konnov and De Ruyck,[9] in accordance with the experimental observation. Consequently, the experimental observation along with the present calculations suggest that the rate of Reaction B8 could not be much lower than the value suggested by Konnov and De Ruyck[9] at these conditions. The gap between the rates of the two routes is shown here to increase with temperature and decrease with pressure. At relatively high pressures and low temperatures, n-N_4H_6 formation becomes significant, yet at the conditions relevant to hydrazine decomposition (1500 K and 25 bar), the formation rate of tetrazane from

N_2H_3 recombination is two orders of magnitude lower than the formation rate of the disproportionation products, $N_2H_4 + N_2H_2(S)$. Also of importance are reactions yielding n-N_3H_4 + NH_2, $NH_2NHN + NH_3$, while formation rates of $NH_2NNH + NH_3$ and i-$N_3H_4 + NH_2$ from the N_2H_3 + N_2H_3 entry channel are negligible (Fig. S11), in accordance with the discussion above.
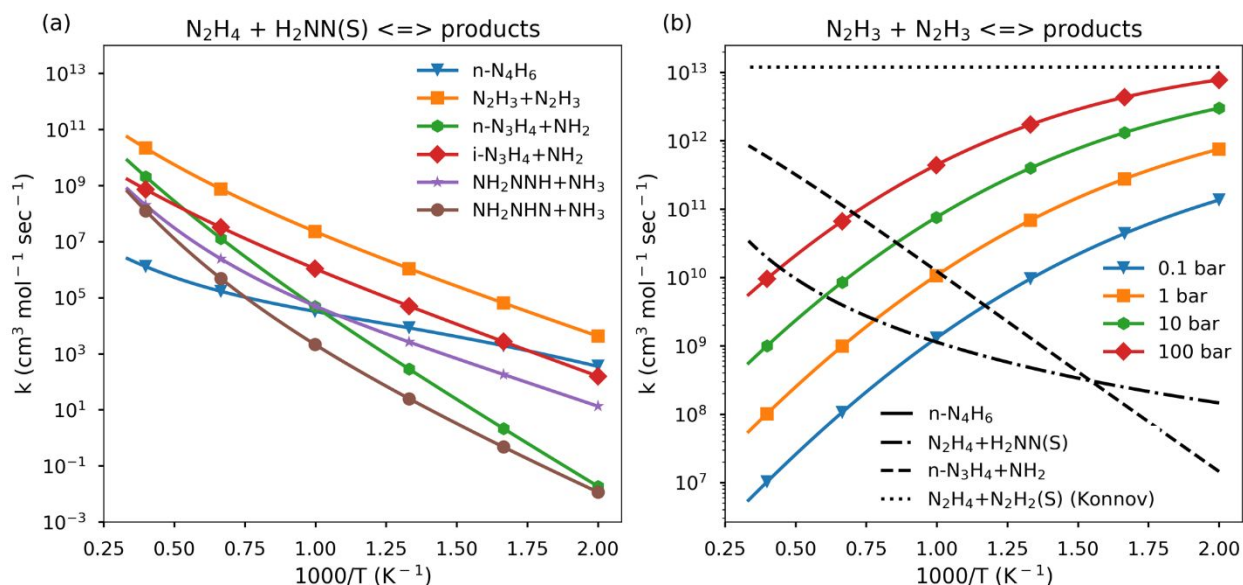

Figure 12. Rate comparisons of $N_2H_4 + H_2NN(S)$ and $N_2H_3 + N_2H_3$ reactions. Rates in (a) are given at a representative pressure of 10 bar. In (b), line types refer to the product/s, while the color refers to the pressure; the pressure-dependence rate for n-$N_3H_4 + NH_2$ formation via a well-skipping reaction is negligible; the rate for $N_2H_4 + H_2NN(S)$ formation includes both a direct route (via TS8) and the well-skipping route; the dotted line is an estimated rate by Konnov and De Ruyck.[9]

3.3. Thermodynamic properties

The present work emphasizes the importance of accounting for triazane (n-N_3H_5) when kinetically studying hydrazine decomposition systems (Fig. 6 c). Tetrazane (n-N_4H_6) formation in this system only becomes important at high pressures and relatively low temperatures (Fig. 12) due to fall-off into $N_2H_3 + N_2H_3$. The main decomposition pathways of triazane are formation of $H_2NN(S) + NH_3$ at high temperatures (Fig. 6 d), as well as hydrogen abstraction reactions due to interactions with the radical pool (mainly H, NH, and N_2H_3). The latter results in the formation of primary or secondary radicals, n-N_3H_4 or i-N_3H_4, respectively (Fig. 9). Preliminary RMG predictions

33

suggest that the n-N_3H_4 radical primarily decomposes into NH_2 + N_2H_2(S) via a beta-scission reaction, while the i-N_3H_4 radical primarily abstracts a hydrogen atom from N_2H_2(S), forming n-N_3H_5 + NNH. Consequently, n-N_3H_5, n-N_3H_4, and i-N_3H_4 should all be considered in future kinetic models of similar systems.

Table 4 Comparison of Relative E0 + ZPE (kJ mol^{-1}) of n-N_3H_5, n-N_3H_4, i-N_3H_4 , and n-N_4H_6 at the CBS-QB3, CCSD(T)-F12a/aug-cc-pVTZ//ωB97x-D3/6-311++G(3df,3pd), and CCSD(T)-F12a/cc-pVTZ-F12//ωB97x-D3/6-311++G(3df,3pd) + BAC Levels of Theory.

species	CBS-QB3	CCSD(T)-F12a/aug-cc-pVTZ	CCSD(T)-F12a/cc-pVTZ-F12 + BAC^a	T1^b
n-N_3H_5	0	0	0	0.0104
n-N_3H_4	125.3	127.5	126.8	0.0234
i-N_3H_4	86.1	89.1	88.2	0.0211
n-N_4H_6	92.3	95.9	96.2	0.0109

^{a} Using bond additivity corrections (BAC)

^{b} The T1 diagnostic parameter,[28] calculated using the CCSD(T)-F12a/aug-cc-pVTZ level of theory

Energies at zero K of n-N_3H_5, n-N_3H_4, i-N_3H_4, and n-N_4H_6 were compared using methods described above, and are given in Table 4. The CCSD(T)-F12a methods consistently predicted energy differences a few kJ mol^{-1} higher than the CBS-QB3 computation, yet well within the reported CBS-QB3 2σ error bar. Thermodynamic properties were computed using Arkane at the CCSD(T)-F12a/cc-pVTZ-F12//ωB97x-D3/6-311++G(3df,3pd) level of theory, implementing rotor scans performed at the B3LYP/6-311++G(3df,3pd) level of theory (Table 5). The n-N_3H_4 and i-N_3H_4 radicals have strong coupling between large amplitude fluxional inversion and a hindered rotor modes (Figs. S6, S7), which makes it challenging to compute their heat capacities. Therefore, only RRHO enthalpies and entropies at 298 K are reported for these radicals.

Table 5 Thermodynamic Properties of n-N_3H_5, n-N_3H_4, i-N_3H_4, and n-N_4H_6 at the CCSD(T)-F12a/cc-pVTZ-F12//ωB97x-D3/6-311++G(3df,3pd) Level of Theory.^{a}

species	ΔH_f^o	ΔS_f^o	$Cp(T)^b$								
			300 K	400 K	500 K	600 K	800 K	1000 K	1500 K	2000 K	2400 K
n-N_3H_5	203.3	276.9	75.1	86.3	95.5	103.7	117.3	128.0	145.7	155.9	161.3
n-N_3H_4	322.5	274.1	–	–	–	–	–	–	–	–	–

34

i-N$_3$H$_4$	289.6	262.7	–	–	–	–	–	–	–	–	–
n-N$_4$H$_6$	299.7	289.8	80.6	99.4	115.2	128.6	150.4	166.6	191.5	205.4	213.3

[a] Enthalpies are given in kJ mol^{-1}, entropies and constant pressure heat capacities are given in J mol^{-1} K^{-1}.

[b] No Cp values are reported for the N$_3$H$_4$ radicals, see text.

The calculated standard heat of formation and entropy of formation of n-N$_3$H$_5$ (Table 5) are comparable with respective past values calculated using the G2 method,[72] 198.7 kJ mol^{-1} and 261.5 J mol^{-1} K^{-1}, respectively.[17] The NASA polynomials for the thermodynamic properties of triazane and tetrazane are given in the Supporting Information.

4. Conclusions

A detailed kinetic analysis of the N$_3$H$_5$ and N$_4$H$_6$ potentials was presented. On the N$_4$H$_6$ potential, the N$_2$H$_4$ + H$_2$NN(S) entry channel mostly yields N$_2$H$_3$ + N$_2$H$_3$, while the N$_2$H$_3$ + N$_2$H$_3$ channel, in turn, would primarily result in the formation of N$_2$H$_4$ + N$_2$H$_2$(S) by direct disproportionation. Overall, hydrazine on this surface mainly catalyzes isomer transformation from H$_2$NN(S) to N$_2$H$_2$(S). At high pressures and low temperatures, tetrazane (n-N$_4$H$_6$) formation becomes significant.

Starting from the N$_2$H$_3$ + NH$_2$ entry channel, all bimolecular product wells on the N$_3$H$_5$ potential can be reached directly via a bimolecular reaction. In fact, the rate contribution of the well-skipping pathway forming N$_2$H$_2$(S) + NH$_3$ to the overall rate is negligible, while the well-skipping route forming H$_2$NN(S) + NH$_3$ has a significant contribution and dominates in the low pressure and low temperature regime. Starting from N$_2$H$_3$ + NH$_2$, H$_2$NN(S) formation is kinetically more favorable than N$_2$H$_2$(S) under 2500 K. However, triazane (n-N$_3$H$_5$) becomes the dominant product of N$_2$H$_3$ + NH$_2$ reaction below 550, 800, 1150, 1250, and 1600 K at 0.1, 1, 10, 25, and 100 bar,

35

respectively. Triazane is predicted to form either $H_2NN(S) + NH_3$ or primary/secondary N_3H_4 radicals, all of which should be taken into consideration in kinetic models of hydrazine.

Theoretical predictions of reaction rates have been derived from ab-initio transition state theory coupled with master equation simulations as necessary. The determined pressure-dependent rates should be of considerable utility to future efforts of kinetic modelling of hydrazine decomposition and related systems.

36

Supporting Information. Transport properties (Table S1), stationary point properties (Table S2), relaxed rotor scans (Figs. S1–S10), branching ratios of $N_2H_3 + N_2H_3$ (Fig. S11), NASA polynomials for n-N_3H_5 and n-N_4H_6, geometric coordinates, and pressure-dependent rates

Acknowledgments

References

(1)   Rothgery, E. F. *Hydrazine and its Derivatives*; 2004; Vol. 13. https://doi.org/10.1002/0471238961.0825041819030809.a01.pub2.

(2)   Gray, P.; Lee, J. C.; Spencer, M. Combustion, Flame and Explosion of Hydrazine and Ammonia I — The Spontaneous Ignition of Pure Gaseous Hydrazine. *Combust. Flame* **1963**, *7*, 315–321. https://doi.org/10.1016/0010-2180(63)90206-2.

(3)   Auzanneau, M.; Roux, M. Self-Detonation Range in Inert Atmosphere of Ternary Systems

37

Using Hydrogen Peroxide and Hydrazine or Hydrazine Derivatives. *Combust. Sci. Technol.* **1990**, *73*, 505–520. https://doi.org/10.1080/00102209008951667.

(4)   *Dynamics of Detonations and Explosions: Detonations*; Leyer, J.-C., Borisov, A. A., Kuhl, A. L., Sirignano, W. A., Eds.; American Institute of Aeronautics and Astronautics: Washington DC, 1991. https://doi.org/10.2514/4.866067.

(5)   Rath, M.; Schmitz, H.; Steenborg, M. Development of a 400 N Hydrazine Thruster for ESA's Atmospheric Reentry Demonstrator. In *32nd Joint Propulsion Conference and Exhibit*; American Institute of Aeronautics and Astronautics: Reston, Virigina, 1996. https://doi.org/10.2514/6.1996-2866.

(6)   Yang, A.-S.; Kuo, T.-C. Design Analysis of a Satellite Hydrazine Propulsion System. *J. Propuls. Power* **2002**, *18*, 270–279. https://doi.org/10.2514/2.5966.

(7)   Anflo, K.; Mollerberg, R.; Neff, K.; King, P. High Performance Green Propellant for Satellite Applications. In *45th AIAA/ASME/SAE/ASEE Joint Propulsion Conference and Exhibit*; American Institute of Aeronautics and Astronautics: Reston, Virigina, 2009. https://doi.org/10.2514/6.2009-4878.

(8)   Halat-Augier, C.; Dupre, G.; Paillard, C. E. Thermal Decomposition of Gaseous Hydrazine behind a Reflected Shock Wave. *Proc. 20th Int. Symp. Shock waves* **1996**, *2*, 893–943.

(9)   Konnov, A. A.; De Ruyck, J. Kinetic Modeling of the Decomposition and Flames of Hydrazine. *Combust. Flame* **2001**, *124*, 106–126. https://doi.org/10.1016/S0010-2180(00)00187-5.

(10)   Hwang, D. Y.; Mebel, A. M. Reaction Mechanism of N_2/H_2 conversion to NH_3: A Theoretical Study. *J. Phys. Chem. A* **2003**, *107*, 2865–2874. https://doi.org/10.1021/jp0270349.

38

(11)   Klippenstein, S. J.; Harding, L. B.; Ruscic, B.; Sivaramakrishnan, R.; Srinivasan, N. K.; Su, M.; Michael, J. V. Thermal Decomposition of NH_2OH and Subsequent Reactions: Ab Initio Transition State Theory and Reflected Shock Tube Experiments. *Society* **2009**, 10241– 10259. https://doi.org/10.1021/jp905454k.

(12)   Asatryan, R.; Bozzelli, J. W.; Da Silva, G.; Swinnen, S.; Tho Nguyen, M. Formation and Decomposition of Chemically Activated and Stabilized Hydrazine. *J. Phys. Chem. A* **2010**, *114*, 6235–6249. https://doi.org/10.1021/jp101640p.

(13)   Wiberg, N.; Bayer, H.; Bachhuber, H. Isolation of Tetrazene, N_4H_4. *Angew. Chemie Int. Ed.* **1975**, *14*, 177–178. https://doi.org/10.1002/anie.197501771.

(14)   Zhao, M.; Gimarc, B. M. Strain Energies of (NH)n Rings, n = 3-8. *J. Phys. Chem.* **1994**, *98*, 7497–7503. https://doi.org/10.1021/j100082a019.

(15)   Inagaki, S.; Ishitani, Y.; Kakefu, T. Geminal Delocalization of .Sigma.-Electrons and Ring Strains. *J. Am. Chem. Soc.* **1994**, *116*, 5954–5958. https://doi.org/10.1021/ja00092a052.

(16)   Ball, D. W. High-Level Ab Initio Calculations on Hydrogen-Nitrogen Compounds. Thermochemistry of Tetrazetidine, N_4H_4. *J. Mol. Struct. THEOCHEM* **2002**, *619*, 37–43. https://doi.org/10.1016/S0166-1280(02)00397-4.

(17)   Schlegel, H. B.; Skancke, A. Thermochemistry, Energy Comparisons, and Conformational Analysis of Hydrazine, Triazane, and Triaminoammonia. *J. Am. Chem. Soc.* **1993**, *115*, 7465–7471. https://doi.org/10.1021/ja00069a053.

(18)   Ball, D. W. Tetrazane: Hartree–Fock, Gaussian-2 and -3, and Complete Basis Set Predictions of Some Thermochemical Properties of N_4H_6. *J. Phys. Chem. A* **2001**, *105*, 465– 470. https://doi.org/10.1021/jp002675u.

39

(19)   Stief, L. J. Ratio of Disproportionation to Combination of N_2H_3 Radicals. *J. Chem. Phys.* **1970**, *52*, 4841–4845. https://doi.org/10.1063/1.1673721.

(20)   Lin, Y.-S.; Li, G.-D.; Mao, S.-P.; Chai, J.-D. Long-Range Corrected Hybrid Density Functionals with Improved Dispersion Corrections. *J. Chem. Theory Comput.* **2013**, *9*, 263–272. https://doi.org/10.1021/ct300715s.

(21)   Krishnan, R.; Binkley, J. S.; Seeger, R.; Pople, J. A. Self-consistent Molecular Orbital Methods. XX. A Basis Set for Correlated Wave Functions. *J. Chem. Phys.* **1980**, *72*, 650–654. https://doi.org/10.1063/1.438955.

(22)   Zimmerman, P. M. Growing String Method with Interpolation and Optimization in Internal Coordinates: Method and Examples. *J. Chem. Phys.* **2013**, *138*, 184102. https://doi.org/10.1063/1.4804162.

(23)   Gonzalez, C.; Schlegel, H. B. An Improved Algorithm for Reaction Path Following. *J. Chem. Phys.* **1989**, *90*, 2154–2161. https://doi.org/10.1063/1.456010.

(24)   Adler, T. B.; Knizia, G.; Werner, H.-J. A Simple and Efficient CCSD(T)-F12 Approximation. *J. Chem. Phys.* **2007**, *127*, 221106. https://doi.org/10.1063/1.2817618.

(25)   Knizia, G.; Adler, T. B.; Werner, H.-J. Simplified CCSD(T)-F12 Methods: Theory and Benchmarks. *J. Chem. Phys.* **2009**, *130*, 054104. https://doi.org/10.1063/1.3054300.

(26)   Dunning, T. H. Gaussian Basis Sets for Use in Correlated Molecular Calculations. I. The Atoms Boron through Neon and Hydrogen. *J. Chem. Phys.* **1989**, *90*, 1007–1023. https://doi.org/10.1063/1.456153.

(27)   Computational Chemistry Comparison and Benchmark Database, National Institute of Standards and Technology (NIST), U.S. Department of Commerce, available online:

40

https://cccbdb.nist.gov/vibscalejust.asp; last accessed: April 2019.

(28)   Lee, T. J.; Rice, J. E.; Scuseria, G. E.; Schaefer, H. F. Theoretical Investigations of Molecules

Composed Only of Fluorine, Oxygen and Nitrogen: Determination of the Equilibrium

Structures of FOOF, $(NO)_2$ and FNNF and the Transition State Structure for FNNF Cis-Trans

Isomerization. *Theor. Chim. Acta* **1989**, *7*5, 81–98. https://doi.org/10.1007/BF00527711.

(29)   Becke, A. D. Density-functional Thermochemistry. III. The Role of Exact Exchange. *J. Chem.*

Phys. **1993**, *98*, 5648–5652. https://doi.org/10.1063/1.464913.

(30)   Gao, C. W.; Allen, J. W.; Green, W. H.; West, R. H. Reaction Mechanism Generator:

Automatic Construction of Chemical Kinetic Mechanisms. *Comput. Phys. Commun.* **2016**,

203, 212–225. https://doi.org/10.1016/j.cpc.2016.02.013.

(31)   2019,   Reaction   Mechanism   Generator,   RMG-Py   v2.3.0,

https://github.com/ReactionMechanismGenerator/RMG-Py.

(32)   Shao, Y.; Gan, Z.; Epifanovsky, E.; Gilbert, A. T. B.; Wormit, M.; Kussmann, J.; Lange, A. W.;

Behn, A.; Deng, J.; Feng, X.; et al. Advances in Molecular Quantum Chemistry Contained in

the   Q-Chem   4   Program   Package.   *Mol.   Phys.*   **2015**,   *113*,   184–215.

https://doi.org/10.1080/00268976.2014.952696.

(33)   Werner, H.-J.; Knowles, P. J.; Knizia, G.; Manby, F. R.; Schütz, M. Molpro: A General-

Purpose Quantum Chemistry Program Package. *Wiley Interdiscip. Rev. Comput. Mol. Sci.*

2012, *2*, 242–253. https://doi.org/10.1002/wcms.82.

(34)   Werner, H.-J.; Knowles, P. J.; Knizia, G.; Manby, F. R.; Schütz, M.; Celani, P.; Györffy, W.;

Kats, D.; Korona, T.; Lindh, R.; et al. Molpro, Version 2015.1, a Package of Ab Initio

Programs. Cardiff, UK 2015.

41

(35)   Frisch, M. J.; Trucks, G. W.; Schlegel, H. B.; Scuseria, G. E.; Robb, M. A.; Cheeseman, J. R.;

       Montgomery, J. A.; Vreven, T.; Kudin, K. N.; Burant, J. C., et al. Gaussian 03, Revision D.01,

       Gaussian, Inc.: Wallingford, Ct, 2009.

(36)   Gilbert, A. IQmol. version 2.11, http://iqmol.org/ 2018.

(37)   Glendening, E. D.; Badenhoop, J. K.; Reed, A. E.; Carpenter, J. E.; Bohmann, J. A.; Morales,

       C. M.; Landis, C. R.; Weinhold, F. NBO 6.0. Theoretical Chemistry Institute, University of

       Wisconsin, Madison (2013).

(38)   Montgomery, J. A.; Frisch, M. J.; Ochterski, J. W.; Petersson, G. A. A Complete Basis Set

       Model Chemistry. VII. Use of the Minimum Population Localization Method. *J. Chem. Phys.*

       2000, *112*, 6532–6542. https://doi.org/10.1063/1.481224.

(39)   Simmie, J. M.; Somers, K. P. Benchmarking Compound Methods (CBS-QB3, CBS-APNO, G3,

       G4, W1BD) against the Active Thermochemical Tables: A Litmus Test for Cost-Effective

       Molecular Formation Enthalpies. *J. Phys. Chem. A* **2015**, *119*, 7235–7246.

       https://doi.org/10.1021/jp511403a.

(40)   Montgomery, J. A.; Frisch, M. J.; Ochterski, J. W.; Petersson, G. A. A Complete Basis Set

       Model Chemistry. VI. Use of Density Functional Geometries and Frequencies. *J. Chem.*

       Phys. **1999**, *110*, 2822–2827. https://doi.org/10.1063/1.477924.

(41)   Bao, J. L.; Zheng, J.; Alecu, I. M.; Lynch, B. J.; Zhao, Y.; D.G., T. Database of Frequency Scale

       Factors   for   Electronic   Model   Chemistries

       https://comp.chem.umn.edu/freqscale/version3b2.htm.

(42)   Alecu, I. M.; Zheng, J.; Zhao, Y.; Truhlar, D. G. Computational Thermochemistry: Scale

       Factor Databases and Scale Factors for Vibrational Frequencies Obtained from Electronic

42

Model Chemistries. *J. Chem. Theory Comput.* **2010**, *6*, 2872–2887. https://doi.org/10.1021/ct100326h.

(43)   Truhlar, D. G.; Garrett, B. C.; Klippenstein, S. J. Current Status of Transition-State Theory. *J. Phys. Chem.* **1996**, *100*, 12771–12800. https://doi.org/10.1021/jp953748q.

(44)   Wong, B. M.; Green, W. H. Effects of Large-Amplitude Torsions on Partition Functions: Beyond the Conventional Separability Assumption. *Mol. Phys.* **2005**, *103*, 1027–1034. https://doi.org/10.1080/00268970412331333627.

(45)   Eckart, C. The Penetration of a Potential Barrier by Electrons. *Phys. Rev.* **1930**, *35*, 1303–1309. https://doi.org/10.1103/PhysRev.35.1303.

(46)   Kislov, V. V.; Mebel, A. M.; Aguilera-Iparraguirre, J.; Green, W. H. Reaction of Phenyl Radical with Propylene as a Possible Source of Indene and Other Polycyclic Aromatic Hydrocarbons: An Ab Initio/RRKM-ME Study. *J. Phys. Chem. A* **2012**, *116*, 4176–4191. https://doi.org/10.1021/jp212338g.

(47)   Allen, J. W.; Goldsmith, C. F.; Green, W. H. Automatic Estimation of Pressure-Dependent Rate Coefficients. *Phys. Chem. Chem. Phys.* **2012**, *14*, 1131–1155. https://doi.org/10.1039/C1CP22765C.

(48)   Goodwin, D. G.; Moffat, H. K.; Speth, R. L. Cantera: An Object-Oriented Software Toolkit for Chemical Kinetics, Thermodynamics, and Transport Processes, 2018. https://doi.org/10.5281/zenodo.170284.

(49)   CHEMKIN-PRO 15131, Reaction Design: San Diego, 2013

(50)   Jasper, A. W.; Miller, J. A. Collisional Energy Transfer in Unimolecular Reactions: Direct Classical Trajectories for $CH_4 \rightleftarrows CH_3 + H$ in Helium. *J. Phys. Chem. A* **2009**, *113*, 5612–5619.

43

https://doi.org/10.1021/jp900802f.

(51)   Jasper, A. W.; Miller, J. A.; Klippenstein, S. J. Collision Efficiency of Water in the Unimolecular Reaction CH_4 (+H_2O) $\leftrightarrows$ CH_3 + H (+H_2O): One-Dimensional and Two-Dimensional Solutions of the Low-Pressure-Limit Master Equation. *J. Phys. Chem. A* **2013**, *117*, 12243–12255. https://doi.org/10.1021/jp409086w.

(52)   Jasper, A. W.; Pelzer, K. M.; Miller, J. A.; Kamarchik, E.; Harding, L. B.; Klippenstein, S. J. Predictive a Priori Pressure-Dependent Kinetics. *Science (80-.).* **2014**, *346*, 1212–1215. https://doi.org/10.1126/science.1260856.

(53)   A.W., J.; M.J., D. Parameterization Strategies for Intermolecular Potentials for Predicting Trajectory-Based Collision Parameters. *J. Chem. Theory Comput.* **2019**, No. submitted.

(54)   Jasper, A. W.; Oana, C. M.; Miller, J. A. "Third-Body" Collision Efficiencies for Combustion Modeling: Hydrocarbons in Atomic and Diatomic Baths. *Proc. Combust. Inst.* **2015**, *35*, 197–204. https://doi.org/10.1016/j.proci.2014.05.105.

(55)   Greenwald, E. E.; North, S. W.; Georgievskii, Y.; Klippenstein, S. J. A Two Transition State Model for Radical–Molecule Reactions: A Case Study of the Addition of OH to C_2H_4. *J. Phys. Chem. A* **2005**, *109*, 6031–6044. https://doi.org/10.1021/jp058041a.

(56)   Jasper, A. W.; Miller, J. A. Theoretical Unimolecular Kinetics for CH_4 + M $\rightleftarrows$ CH_3 + H + M in Eight Baths, M = He, Ne, Ar, Kr, H_2 , N_2 , CO, and CH_4. *J. Phys. Chem. A* **2011**, *115*, 6438–6455. https://doi.org/10.1021/jp200048n.

(57)   Klippenstein, S. J.; Miller, J. A.; Jasper, A. W. Kinetics of Propargyl Radical Dissociation. *J. Phys. Chem. A* **2015**, *119*, 7780–7791. https://doi.org/10.1021/acs.jpca.5b01127.

(58)   Tranter, R. S.; Jasper, A. W.; Randazzo, J. B.; Lockhart, J. P. A.; Porterfield, J. P.

44

Recombination and Dissociation of 2-Methyl Allyl Radicals: Experiment and Theory. *Proc. Combust. Inst.* **2017**, *36*, 211–218. https://doi.org/10.1016/j.proci.2016.06.040.

(59)   Jasper, A. W.; Miller, J. A. Lennard–Jones Parameters for Combustion and Chemical Kinetics Modeling from Full-Dimensional Intermolecular Potentials. *Combust. Flame* **2014**, *161*, 101–110. https://doi.org/10.1016/j.combustflame.2013.08.004.

(60)   Jasper, A. W.; Kamarchik, E.; Miller, J. A.; Klippenstein, S. J. First-Principles Binary Diffusion Coefficients for H, H_2 , and Four Normal Alkanes + N_2. *J. Chem. Phys.* **2014**, *141*, 124313. https://doi.org/10.1063/1.4896368.

(61)   Zhang, P.; Klippenstein, S. J.; Sun, H.; Law, C. K. Ab Initio Kinetics for the Decomposition of Monomethylhydrazine (CH_3NHNH_2). *Proc. Combust. Inst.* **2011**, *33*, 425–432. https://doi.org/10.1016/j.proci.2010.05.010.

(62)   Förstel, M.; Tsegaw, Y. A.; Maksyutenko, P.; Mebel, A. M.; Sander, W.; Kaiser, R. I. On the Formation of N_3H_3 Isomers in Irradiated Ammonia Bearing Ices: Triazene (H_2NNNH) or Triimide (HNHNNH). *ChemPhysChem* **2016**, *17*, 2726–2735. https://doi.org/10.1002/cphc.201600414.

(63)   Dean, A. M.; Bozzelli, J. W. Combustion Chemistry of Nitrogen. In *Gas-Phase Combustion Chemistry*; Springer New York: New York, NY, 2000; pp 125–341. https://doi.org/10.1007/978-1-4612-1310-9_2.

(64)   Mulliken, R. S. Electronic Population Analysis on LCAO–MO Molecular Wave Functions. I. *J. Chem. Phys.* **1955**, *23*, 1833–1840. https://doi.org/10.1063/1.1740588.

(65)   Chang, A. Y.; Bozzelli, J. W.; Dean, A. M. Kinetic Analysis of Complex Chemical Activation and Unimolecular Dissociation Reactions Using QRRK Theory and the Modified Strong

45

Collision Approximation. *Zeitschrift für Phys. Chemie* **2000**, *214*, 1533. https://doi.org/10.1524/zpch.2000.214.11.1533.

(66) Simmie, J. M. A Database of Formation Enthalpies of Nitrogen Species by Compound Methods (CBS-QB3, CBS-APNO, G3, G4). *J. Phys. Chem. A* **2015**, *119*, 10511–10526. https://doi.org/10.1021/acs.jpca.5b06054.

(67) Bugler, J.; Somers, K. P.; Simmie, J. M.; Güthe, F.; Curran, H. J. Modeling Nitrogen Species as Pollutants: Thermochemical Influences. *J. Phys. Chem. A* **2016**, *120*, 7192–7197. https://doi.org/10.1021/acs.jpca.6b05723.

(68) Hanson, R. K.; Salimian, S. Survey of Rate Constants in the N/H/O System. In *Combustion Chemistry*; Springer New York: New York, NY, 1984; pp 361–421. https://doi.org/10.1007/978-1-4684-0186-8_6.

(69) Klippenstein, S. J.; Miller, J. A. From the Time-Dependent, Multiple-Well Master Equation to Phenomenological Rate Coefficients. *J. Phys. Chem. A* **2002**, *106*, 9267–9277. https://doi.org/10.1021/jp021175t.

(70) Miller, J. A.; Klippenstein, S. J. Master Equation Methods in Gas Phase Chemical Kinetics. *J. Phys. Chem. A* **2006**, *110*, 10528–10544. https://doi.org/10.1021/jp062693x.

(71) Prozument, K.; Suleimanov, Y. V.; Buesser, B.; Oldham, J. M.; Green, W. H.; Suits, A. G.; Field, R. W. A Signature of Roaming Dynamics in the Thermal Decomposition of Ethyl Nitrite: Chirped-Pulse Rotational Spectroscopy and Kinetic Modeling. *J. Phys. Chem. Lett.* **2014**, *5*, 3641–3648. https://doi.org/10.1021/jz501758p.

(72) Curtiss, L. A.; Raghavachari, K.; Trucks, G. W.; Pople, J. A. Gaussian-2 Theory for Molecular Energies of First- and Second-row Compounds. *J. Chem. Phys.* **1991**, *94*, 7221–7230.

46

47

1
2
3
4
5
6
7
8
9
10
11
12
13
14
15
16
17
18
19
20
21
22
23
24
25
26
27
28
29
30
31
32
33
34
35
36
37
38
39
40
41
42
43
44
45
46
47
48
49
50
51
52
53
54
55
56
57
58
59
60

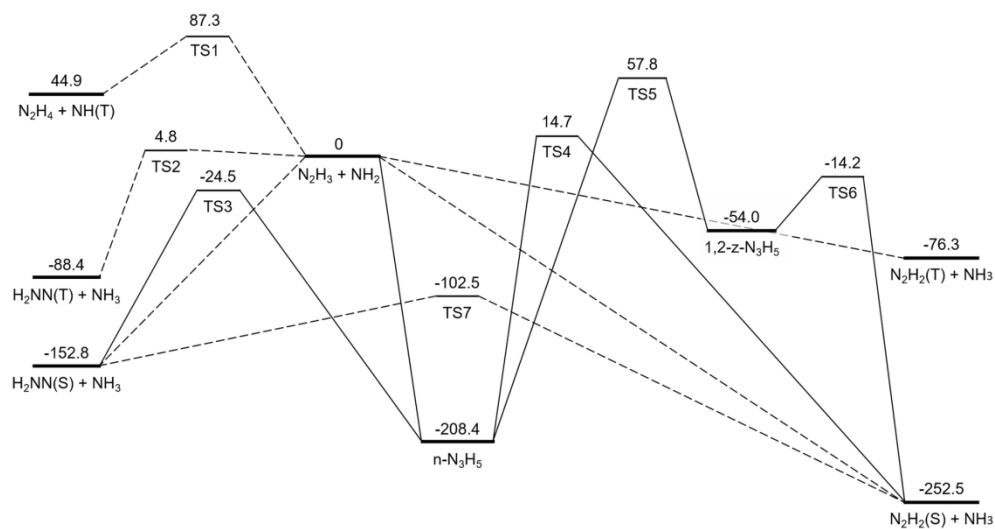**Table of Contents Graphic**
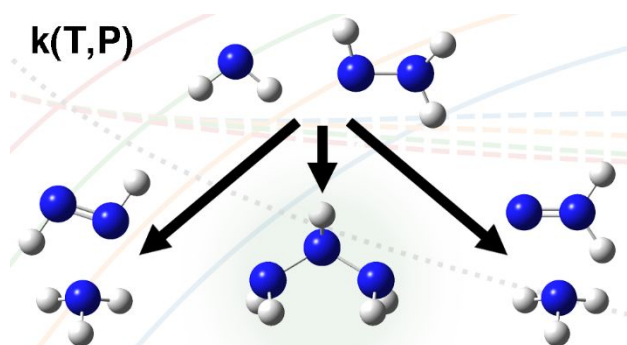
48

Figure 1. Reaction path diagram for the N_3H_5 PES. Dashed lines represent non-pressure-dependent pathways. (S) and (T) represent singlet or triplet multiplicities, respectively. Energies are in kJ mol^{-1}, and scaled relative to the $N_2H_3 + NH_2$ entry channel, which was set at zero.

177x94mm (300 x 300 DPI)
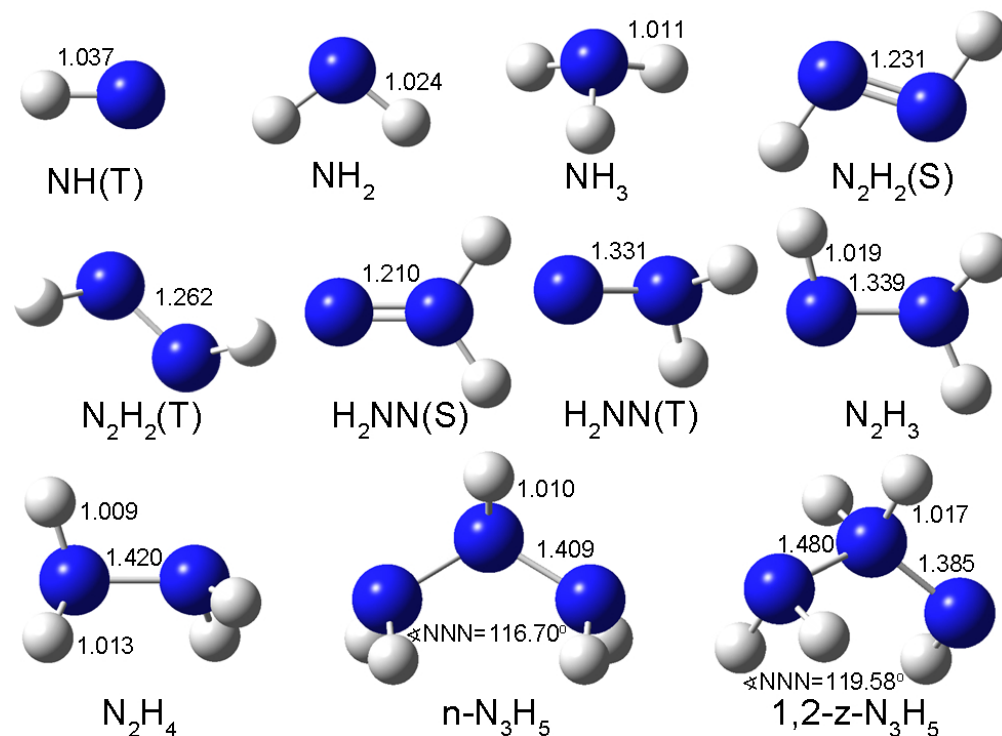
1
2
3
4
5
6
7
8
9
10
11
12
13
14
15
16
17
18
19
20
21
22
23
24
25
26
27
28
29
30
31
32
33
34
35
36
37
38
39
40
41
42
43
44
45
46
47
48
49
50
51
52
53
54
55
56
57
58
59
60

Figure 2. Geometric representation of species on the N_3H_5 PES optimized at the ωB97x-D3/6-311++G(3df,3pd) level of theory. Bond orders shown for illustration purpose only. Bond lengths are in Å and angles in degrees. Quantitative geometric data was added where it benefits the discussion; geometric coordinates for all species are available in the Supporting Information.

Figure 3. Geometric representation of transition states on the N_3H_5 PES optimized at the ωB97x-D3/6-311++G(3df,3pd) level of theory. Bond lengths are in Å and angles in degrees. Numbers in parentheses indicate the bond stretch fraction relative to the respective stable species. Quantitative geometric data was added where it benefits the discussion; geometric coordinates for all transition states are available in the Supporting Information.
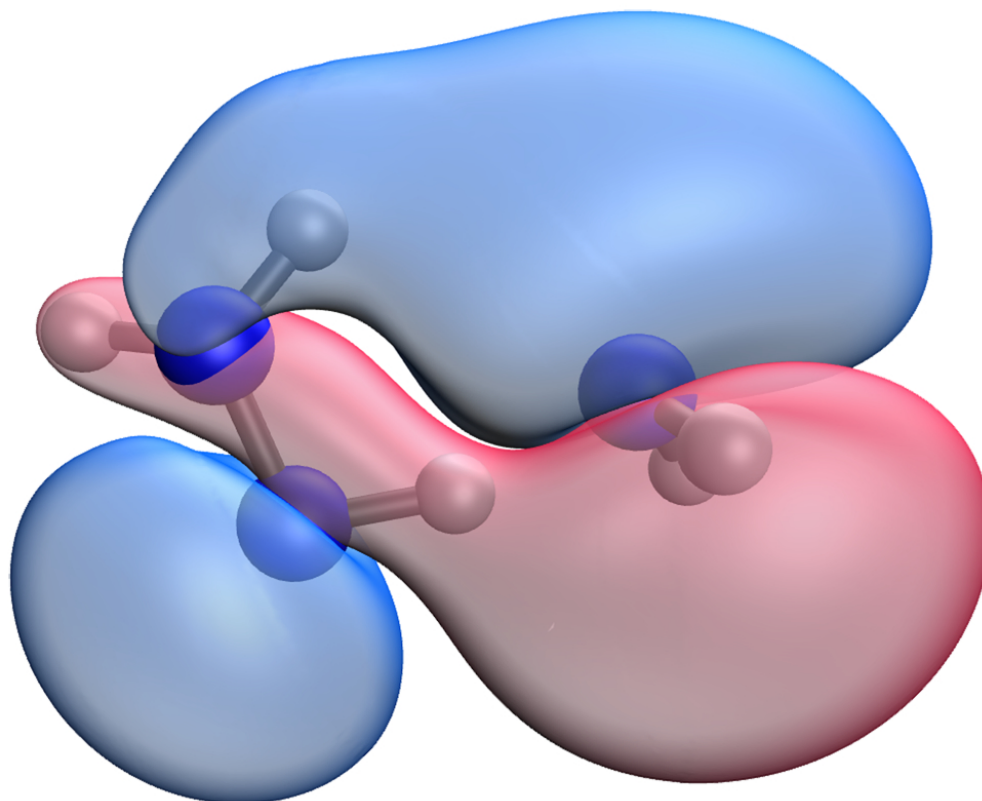
Figure 4. Highest alpha-electron occupied molecular orbital (MO 12) in the triplet saddle point TS2, computed at the ωB97x-D3/6-311++G(3df,3pd) level of theory.

82x67mm (300 x 300 DPI)
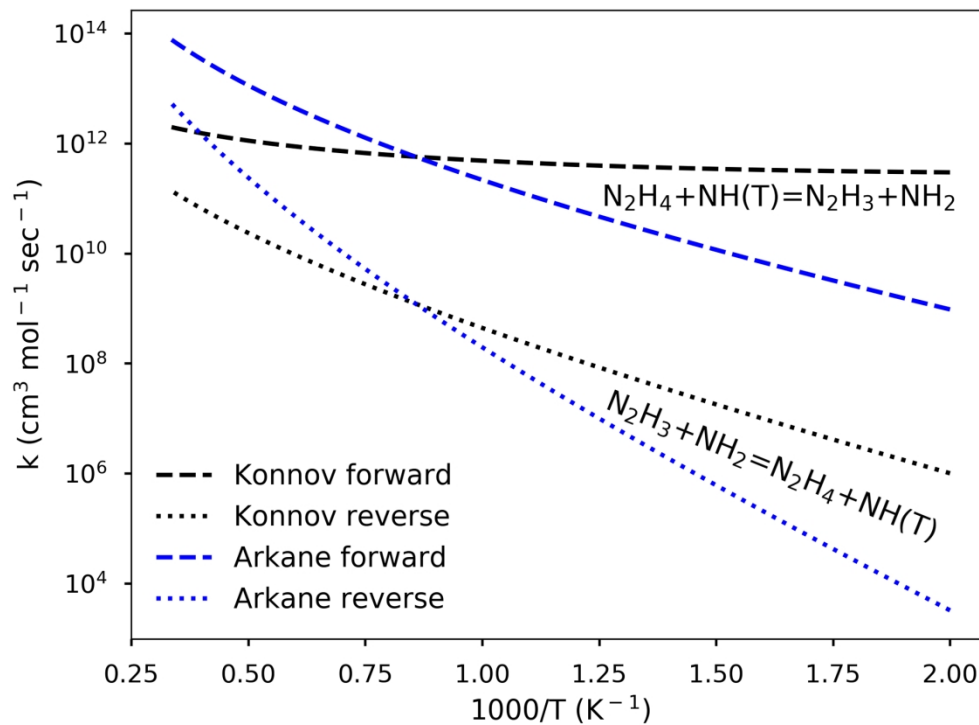
1
2
3
4
5
6
7
8
9
10
11
12
13
14
15
16
17
18
19
20
21
22
23
24
25
26
27
28
29
30
31
32
33
34
35
36
37
38
39
40
41
42
43
44
45
46
47
48
49
50
51
52
53
54
55
56
57
58
59
60

Figure 5. Rate comparisons of Reaction R1 (forward) and R-1 (reverse) between the present work calculation using Arkane and the rate estimated and reported by Konnov and De Ruyck.[9] Thermodynamic data from Curran et al.[65] was used to compute reverse rates.

177x129mm (300 x 300 DPI)
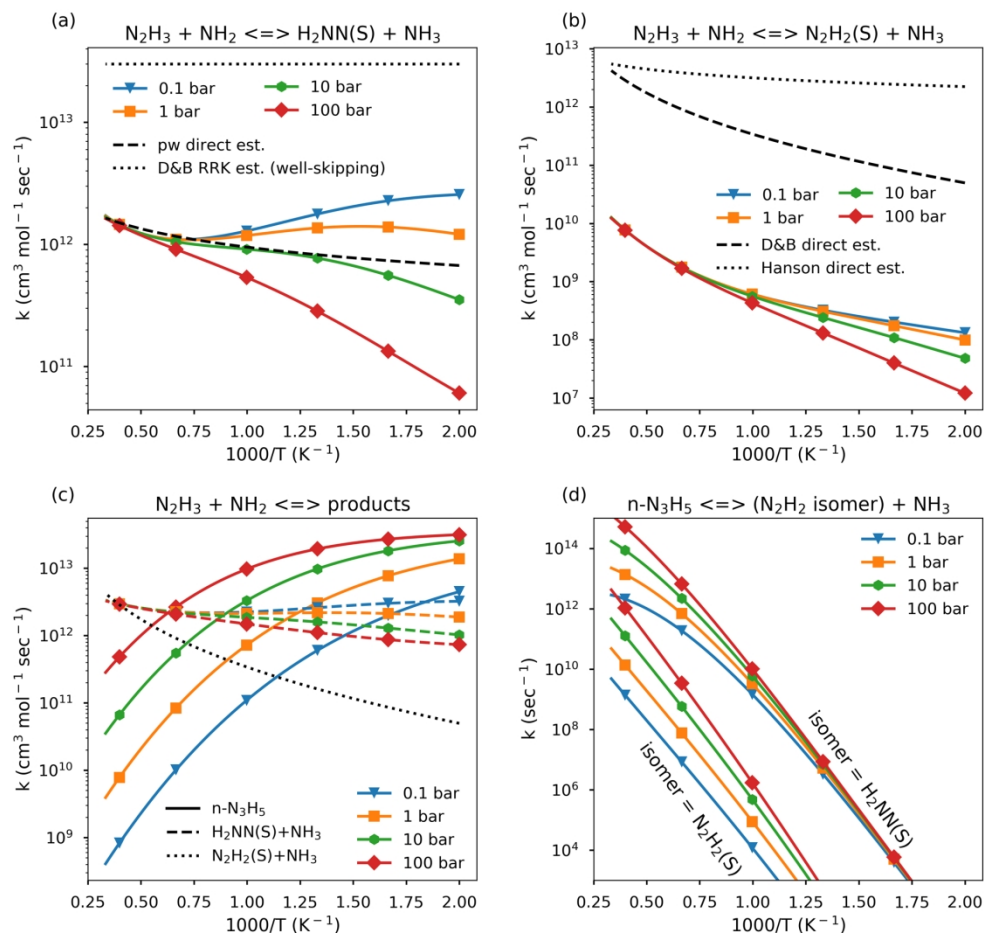
Figure 6. Rate comparisons of selected reactions on the N_3H_5 PES. 'D&B' in the legend refers to the book chapter by Dean and Bozzelli from 2000,[61] and 'Hanson' refers to a N/H/O rate constants review by Hanson and Salimian from 1984.[66] Present work is denoted as 'pw'. In (c), line types refer to the product/s, while the color refers to the pressure; the pressure-dependence of the $N_2H_2(S)$ + NH_3 formation rate is negligible, while formation rates of $H_2NN(S)$ + NH_3 include both pressure-dependent and direct routes; the updated Dean and Bozzelli rate for $N_2H_2(S)$ + NH_3 is shown.
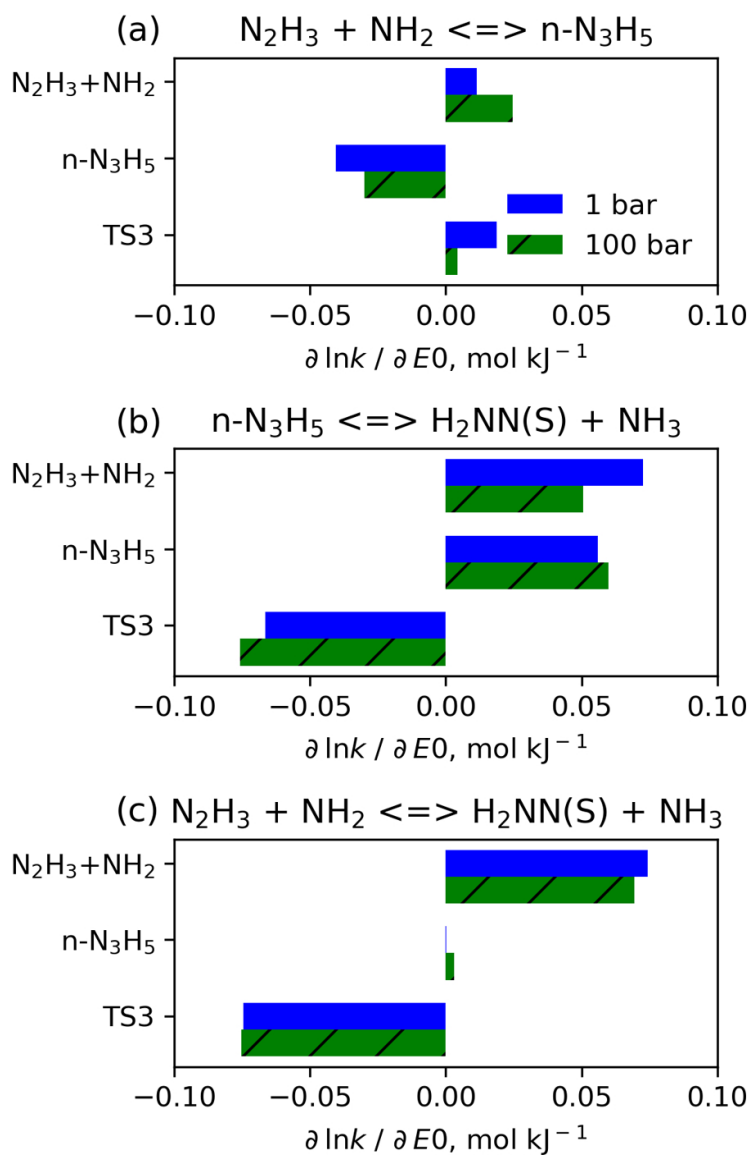
Figure 7. Normalized sensitivity coefficients to ZPE-corrected energies of $N_2H_3 + NH_2$, n-N_3H_5, and TS3 for selected pressure-dependent rates on the N_3H_5 potential at 1 and 100 bar and at 1500 K.
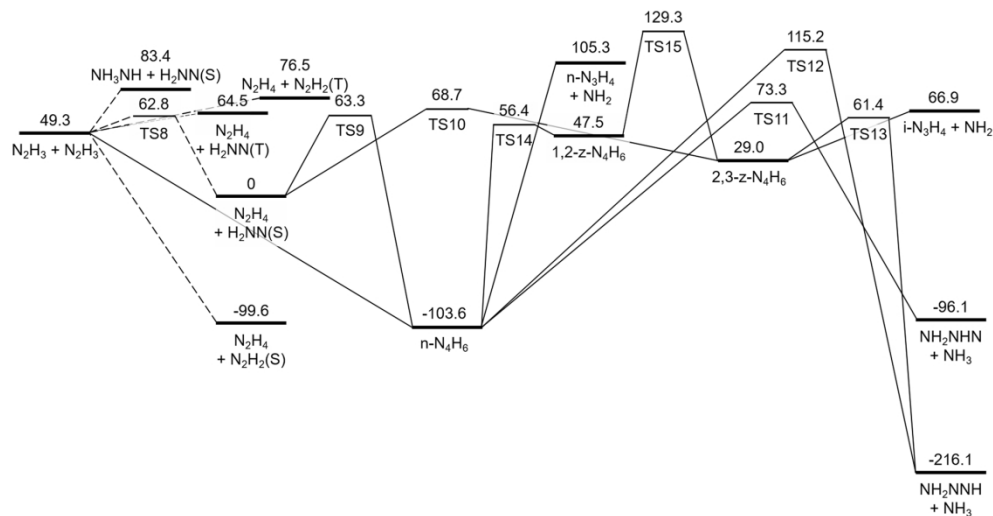
82x123mm (300 x 300 DPI)

Figure 8. Reaction path diagram for the N_4H_6 potential. Dashed lines represent non-pressure-dependent pathways. (S) and (T) represent singlet or triplet multiplicities, respectively. Energies are in kJ mol^{-1}, and scaled relative to the $N_2H_4 + H_2NN$(S) entry channel, which was set at zero.
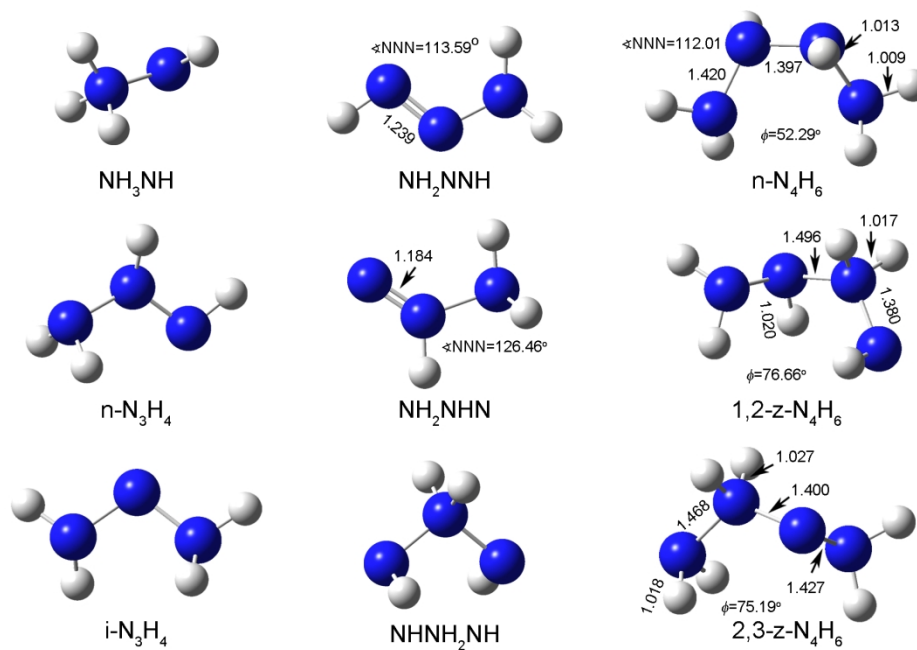
177x93mm (300 x 300 DPI)

Figure 9. Geometric representation of species on the N_4H_6 PES optimized at the ωB97x-D3/6-311++G(3df,3pd) level of theory. Species already given in Fig. 2 were not reproduced here. Bond orders shown for illustration purpose only. Bond lengths are in Å and angles in degrees. Φ is the dihedral angle between the four nitrogen backbone atoms. Quantitative geometric data was added where it benefits the discussion; geometric coordinates for all species are available in the Supporting Information.
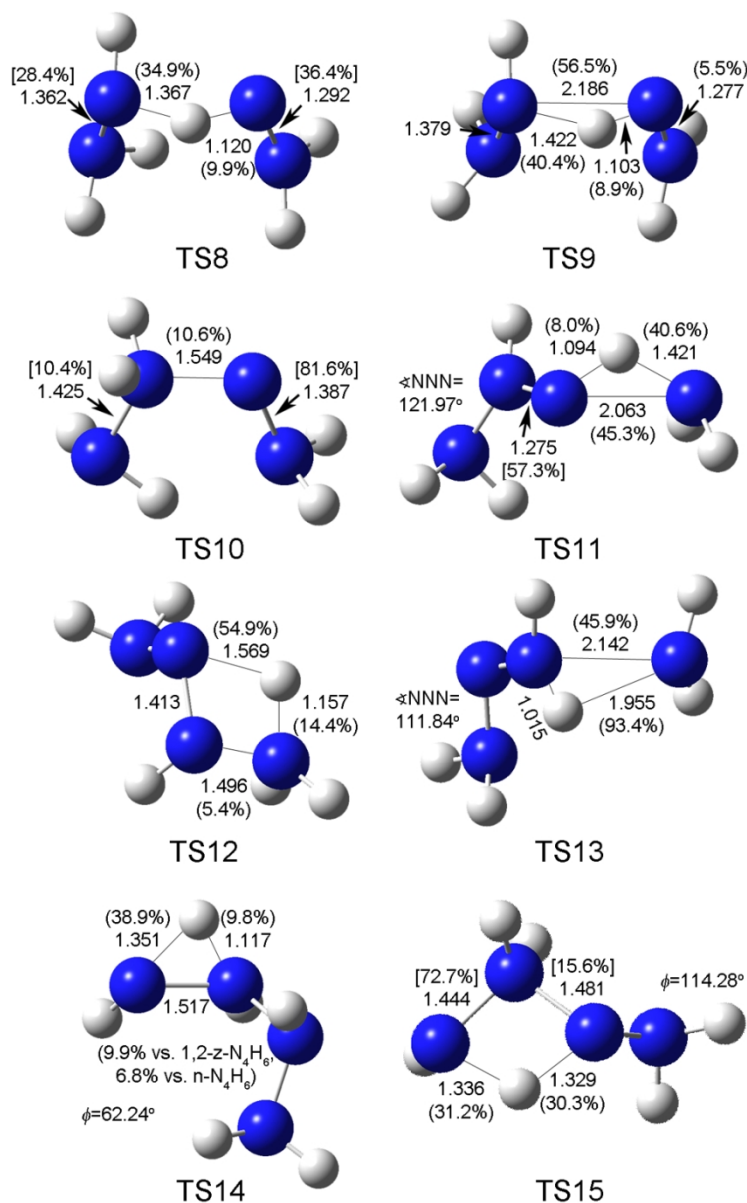
Figure 10. Geometric representation of transition states on the N_4H_6 PES optimized at the ωB97x-D3/6-311++G(3df,3pd) level of theory. Bond lengths are in Å and angles in degrees. Numbers in parentheses indicate the bond stretch fraction relative to the respective stable species. Numbers in brackets indicate the relative bond stretch fraction out of the total change between the respective reactant and product in the direction specified in Table 3. Φ is the dihedral angle between the four nitrogen backbone atoms. Quantitative geometric data was added where it benefits the discussion; geometric coordinates for all transition states are available in the Supporting Information.
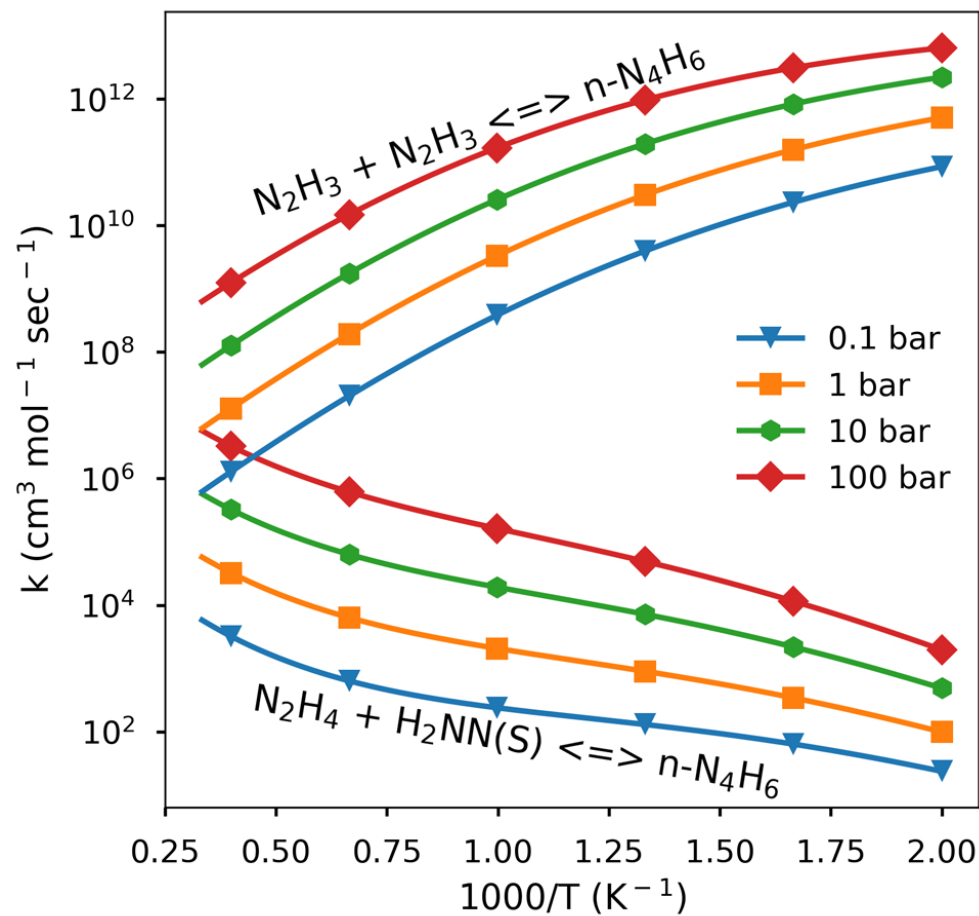
Figure 11. Rate coefficient comparison of n-N_4H_6 formation from each of the entry channels as a function of temperature and pressure.

82x80mm (300 x 300 DPI)

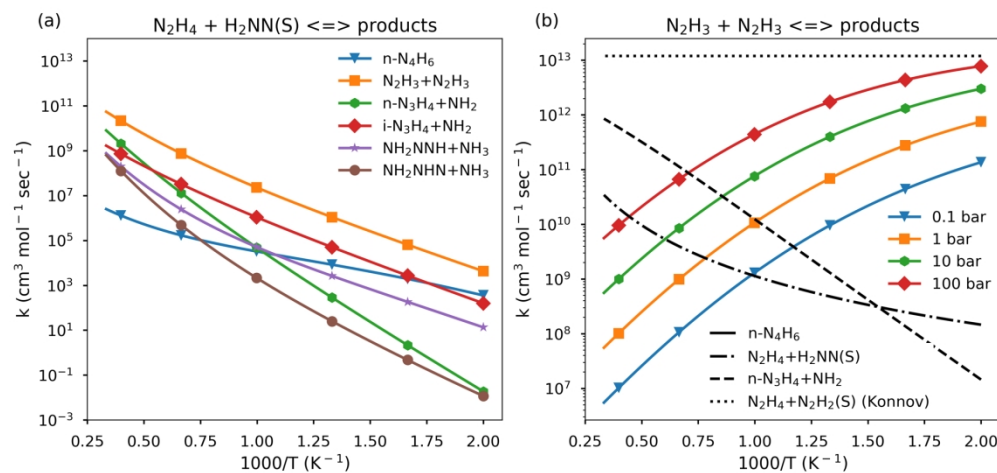**Figure 12.** Rate comparisons of $N_2H_4 + H_2NN(S)$ and $N_2H_3 + N_2H_3$ reactions. Rates in (a) are given at a representative pressure of 10 bar. In (b), line types refer to the product/s, while the color refers to the pressure; the pressure-dependence rate for $n\text{-}N_3H_4 + NH_2$ formation via a well-skipping reaction is negligible; the rate for $N_2H_4 + H_2NN(S)$ formation includes both a direct route (via TS8) and the well-skipping route; the dotted line is an estimated rate by Konnov and De Ruyck.[9]